

Alma Mater Studiorum Università di Bologna
Archivio istituzionale della ricerca

Hydrothermal silicification and hypogene dissolution of an exhumed Neoproterozoic carbonate sequence in Brazil: Insights from fluid inclusion microthermometry and silicon-oxygen isotopes

This is the final peer-reviewed author's accepted manuscript (postprint) of the following publication:

Published Version:

Pisani L., Koltai G., Dublyansky Y., Kleine B.I., Whitehouse M.J., Skrzypek E., et al. (2023). Hydrothermal silicification and hypogene dissolution of an exhumed Neoproterozoic carbonate sequence in Brazil: Insights from fluid inclusion microthermometry and silicon-oxygen isotopes. BASIN RESEARCH, Early Access, 1-26 [10.1111/bre.12748].

Availability:

This version is available at: <https://hdl.handle.net/11585/919380> since: 2024-05-17

Published:

DOI: <http://doi.org/10.1111/bre.12748>

Terms of use:

Some rights reserved. The terms and conditions for the reuse of this version of the manuscript are specified in the publishing policy. For all terms of use and more information see the publisher's website.

This item was downloaded from IRIS Università di Bologna (<https://cris.unibo.it/>).
When citing, please refer to the published version.

(Article begins on next page)

This is the final peer-reviewed accepted manuscript of:

Pisani, L., Koltai, G., Dublyansky, Y., Kleine, B. I., Whitehouse, M. J., Skrzypek, E., . . . De Waele, J. (2022). Hydrothermal silicification and hypogene dissolution of an exhumed neoproterozoic carbonate sequence in Brazil: Insights from fluid inclusion microthermometry and silicon-oxygen isotopes. Basin Research

The final published version is available online at
<https://dx.doi.org/10.1111/bre.12748>

Terms of use:

Some rights reserved. The terms and conditions for the reuse of this version of the manuscript are specified in the publishing policy. For all terms of use and more information see the publisher's website.

This item was downloaded from IRIS Università di Bologna (<https://cris.unibo.it/>)

When citing, please refer to the published version.

Hydrothermal silicification and hypogene dissolution of an exhumed Neoproterozoic carbonate sequence in Brazil: Insights from fluid inclusion microthermometry and silicon-oxygen isotopes

Luca Pisani^{1*}, Gabriella Koltai², Yuri Dublyansky², Barbara I. Kleine³, Martin J. Whitehouse⁴, Etienne Skrzypek⁵, Cristina Carbone⁶, Christoph Spötl², Marco Antonellini¹, Francisco H. Bezerra⁷, Jo De Waele¹

¹ Bologna University, Department of Biological, Geological and Environmental Sciences, Italy. lucapiso94@gmail.com; m.antonellini@unibo.it; jo.dewaele@unibo.it

² Institute of Geology, University of Innsbruck, Austria. Gabriella.Koltai@uibk.ac.at; Yuri.Dublyansky@uibk.ac.at; Christoph.Spoetl@uibk.ac.at

³ Nordic Volcanological Center, Institute of Earth Sciences, University of Iceland. barbarak@hi.is

⁴ Swedish Museum of Natural History, Stockholm, Sweden, martin.whitehouse@nrm.se

⁵ Institute of Earth Sciences, NAWI Graz Geozentrum, Petrology and Geochemistry, University of Graz, Austria. etienne.skrzypek@uni-graz.at

⁶ DISTAV, Dipartimento di Scienze della Terra, dell'Ambiente e della Vita, Università di Genova, Italy. cristina.carbone@unige.it

⁷ Programa de Pós-Graduação em Geodinâmica e Geofísica, Federal University of Rio Grande Do Norte, Natal, Brazil. hilario.bezerra@ufrn.br

Corresponding author

Abstract

Hypogene dissolution-precipitation processes strongly affect petrophysical properties of carbonate rocks and fluid migration pathways in sedimentary basins. In many deep carbonate reservoirs, hypogene cavernous voids are often associated with silicified horizons. The diagenesis of silica in carbonate sequences is still a poorly-investigated research topic. Studies exploring the complexity of silica dissolution-precipitation patterns in hypogene cave analogues are therefore fundamental to unravel the diagenetic and speleogenetic processes that may affect this kind of reservoirs. In this work we investigated an exhumed and silicified Neoproterozoic carbonate sequence in Brazil hosting a 1.4 km-long cave. Quartz mineralization and silicified textures were analyzed with a

This article has been accepted for publication and undergone full peer review but has not been through the copyediting, typesetting, pagination and proofreading process which may lead to differences between this version and the [Version of Record](https://doi.org/10.1111/bre.12748). Please cite this article as doi: [10.1111/bre.12748](https://doi.org/10.1111/bre.12748)

multidisciplinary approach combining petrography, fluid inclusion microthermometry, silicon-oxygen stable isotope analyses, and U-Th-Pb dating of monazite crystals. We found that an early silicification event caused the replacement of the dolostone layers with micro-crystalline quartz forming chert nodules. This event was likely associated with mixing fluids (ancient Neoproterozoic seawater and hydrothermal solutions sourced from the underlying Mesoproterozoic basement) at relatively low temperatures (ca. 50-100 °C) and shallow depth. After the tectonic deformation produced by the Brasiliano orogeny, silica dissolution was promoted by high temperature and alkaline hydrothermal solutions rising from the quartzite basement along deep-rooted structures. Hypogene hydrothermal alteration promoted the dissolution of the cherty layers and the precipitation of chalcedony and megaquartz. Homogenization temperatures from primary fluid inclusions in megaquartz cement indicate minimum formation temperatures of 165-210 °C. Similar temperature estimates (110-200 °C) were obtained from the $\delta^{30}\text{Si}$ and $\delta^{18}\text{O}$ isotope systematics of quartz precipitated from hydrothermal solutions. The dissolved salts in the fluid inclusions were evaluated as $\text{NaCl}+\text{CaCl}_2$ from microthermometric data combined with cryogenic Raman spectroscopy, corresponding to salinity ranging between 17 and 25 wt.%. No reliable age constraints for hydrothermal silica dissolution-precipitation phases were obtained from monazite U-Th-Pb dating. However, our results, interpreted in the regional context of the São Francisco Craton, suggest that the Cambrian tectono-thermal events could have been among the possible drivers for this hypogene process in the basin.

Key words

Silicified reservoirs; fluid flow; hydrothermal karst; silica dissolution

1. Introduction

Although solubility of silica under most surface or shallow crustal conditions is low (Rimstidt, 1997), dissolution (karstic) features including caves and cave systems are known in quartz-dominated rocks (Sauro et al., 2014; Wray and Sauro, 2017). Solutional voids and karstic vugs are commonly found in quartzites and silicified (cherty) carbonates in many hydrocarbon reservoirs in sedimentary basins, such as North Slope in Alaska (e.g., Shanmugan and Higgins, 1988), offshore Brazil (De Luca et al., 2017; Lima et al., 2020; Fernández-Ibáñez et al., 2022a), and Tarim Basin in China (Dong et al., 2018; You et al., 2018; Wei et al., 2021).

Karst features in deep reservoirs are commonly attributed to hypogene dissolution (hypogene speleogenesis) resulting from upwelling and migration of thermal groundwaters (Dublyansky, 1990; Andreychouk et al., 2009; Klimchouk, 2007; 2019). Hydrothermal alteration in carbonate reservoirs resulting in cavernous vugs and non-matrix permeability is a common phenomenon, especially along fault and fracture zones (Álvaro, 2013; Zhou et al., 2014; Fernández-Ibáñez et al., 2022a; Strugale and Cartwright, 2022). These hypogene karst processes generate non-fabric-selective interconnected pore systems, resulting in heterogeneous porosity and highly anisotropic rock permeability (Trice, 2005; Fernández-Ibáñez et al., 2022a), which has implications not only for hydrocarbon exploration but also for the characterization of geothermal resources and groundwater reserves (Goldscheider et al., 2010; Montanari et al., 2017; Audra et al., 2022).

Exhumed hypogene caves accessible from the surface represent analogues of deep-seated conduit systems, where parameters of cave-forming environments can be reconstructed by studying mineralogical and geochemical footprints (Klimchouk, 2019). Studies of such features-analogues of deep-seated conduits are indispensable for interpreting data from drilling and geophysical surveys and building accurate conceptual models.

An increasing number of publications have documented the development of hypogene caves and karst features in silicified carbonate rocks (Sauro et al., 2014; Bertotti et al., 2020; La Bruna et al., 2021; Souza et al., 2021; Pisani et al., 2022). Cavernous, sometimes mineralized solutional voids attributed to hydrothermal speleogenesis have been described in quartzites and skarns in Kyrgyzstan (Leven, 1961; Kornilov, 1978), USA (Colorado; Lovering et al., 1978), and Ukraine (Tsykin, 1989). Silicified reservoirs are typical of the lower Cretaceous pre-salt sequences of the Campos and Santos basins in Brazil (Lima and De Ros, 2019; Lima et al., 2020), the Kwanza-Congo Basins of Africa (Poros et al., 2017; Teboul et al., 2019), and the Parkland gas field in Canada (Packard et al., 2001). On the basis of petrographic, isotopic, and fluid inclusion studies, pervasive silicification and porosity enhancement processes in these basins were ascribed to the circulation of high-temperature fluids (Girard and San Miguel, 2017; De Luca et al., 2017; Poros et al., 2017; Teboul et al., 2019; Lima et al., 2020). However, the link between silicification and hypogene karst dissolution, and their evolution in space and time, are still poorly understood.

The study of secondary minerals lining or filling solutional (karstic) cavities is a powerful tool that can be combined with geomorphological observations to build accurate speleogenetic and minerogenetic models (Onac and Forti, 2011). Understanding properties and origin of hydrothermal mineralizations (e.g., by studying fluid inclusions, stable isotopes, and trace elements) may provide

new insights into the characterization of hypogene conduit networks associated with ore deposit emplacement, hydrocarbon reservoirs, and geothermal resources.

In this paper we present the results of the study of an inactive hypogene cave system (Calixto Cave) developed in the Neoproterozoic rocks of the Una-Utinga Basin in northeastern Brazil. Using a multidisciplinary approach comprising petrographic, stratigraphic, structural, and geomorphological observations, Pisani et al. (2022) documented quartz-rich mineral deposits partially filling solutional pores and fractures in the silicified rocks that host the main corroded high-permeability zones of the sedimentary sequence.

Since various processes may be involved in the formation of quartz-rich mineralization and silicified layers in marine carbonate units, a detailed characterization of quartz textures and mineral-forming fluid properties is needed to understand the character and evolution of fluid circulation, fluid-rock interaction, and silica dissolution-precipitation.

To unravel the origin of silica dissolution-precipitation processes, we combined petrographic observations with fluid-inclusion studies and silicon ($\delta^{30}\text{Si}$) and oxygen ($\delta^{18}\text{O}$) isotope analyses of quartz, chalcedony, and highly silicified chert samples from Calixto Cave, and quartzite samples from the underlying Mesoproterozoic basement (Chapada Diamantina Group). These analyses were integrated with the U-Th-Pb dating of monazite grains found in association with quartz-rich mineralization, attempting to constrain the age for fluid circulation, speleogenesis, and mineral deposition. Lastly, the Si and O isotope composition of studied materials was compared with different genetic mechanisms using an isotope modelling approach (Stefánsson et al., 2017; Kleine et al., 2018).

2. Geological setting

The Calixto Cave is located in the São Francisco Craton (northeastern Brazil, Fig. 1a). This hypogene karst system comprises 1.4 km of passages located between 420 and 475 m a.s.l. and is developed in the Neoproterozoic carbonates of the Salitre Formation (Fm), Una-Utinga Basin.

The São Francisco Craton is the western portion of a large crustal block segmented during the breakup of Pangea (Almeida et al., 2000; Misi et al., 2011). The Neoproterozoic rocks of the Una Group (Misi et al., 2007, 2011) overlay the Archean-Paleoproterozoic basement, comprised of metamorphic and igneous rocks, and the mainly siliciclastic Mesoproterozoic sequences of the Chapada Diamantina Group, rich in quartzites and ortho-quartzites (Magalhães et al., 2016) (Fig. 1b). The Una-Utinga and the Irecê basins resulted from the rifting of the Rodinia supercontinent between ca. 900 to 600 Ma (Misi and Veizer, 1998; Misi et al., 2007, 2011). This extensional stage

was responsible for the sedimentation of glaciogenic and marine carbonate mega-sequences of the Una Group.

Sedimentation in these basins was partially coeval with the geodynamic and tectonic events of the Brasiliano orogeny, which occurred in this area from ca. 740 to 540 Ma with a peak at 600 Ma (Brito Neves et al., 2014; Bento dos Santos et al., 2015; Sial et al., 2016; Santana et al., 2021). A first rifting event and a subsequent collisional stage determined the present structural configuration of the basins, with thrust faults, strike-slip (or oblique-slip) faults, and folded belts (Brito Neves et al., 2014; D'Angelo et al., 2019). The late orogenic stages (540–510 Ma) involved magmatism, hydrothermal activity, and large-scale fluid migration along faults and shear zones (Almeida et al., 2000; Trindade et al., 2004; Guimarães et al., 2011).

The lower units of the Salitre Fm are interpreted as the product of accumulation of sediments in an intra-cratonic basin during rifting of the passive northern margin of the craton (Misi and Veizer, 1998; Misi et al., 2007; Santana et al., 2021). The upper part of the Salitre Fm is considered by some authors as a foreland basin filled with mega-sequences deposited during the Brasiliano orogeny ca. 600 Ma ago (Misi et al., 2007, 2011; Santana et al., 2021). The maximum depositional age determined from detrital zircons in the basal portion of the Salitre Fm is 669 ± 14 Ma (Sial et al., 2016; Santana et al., 2021).

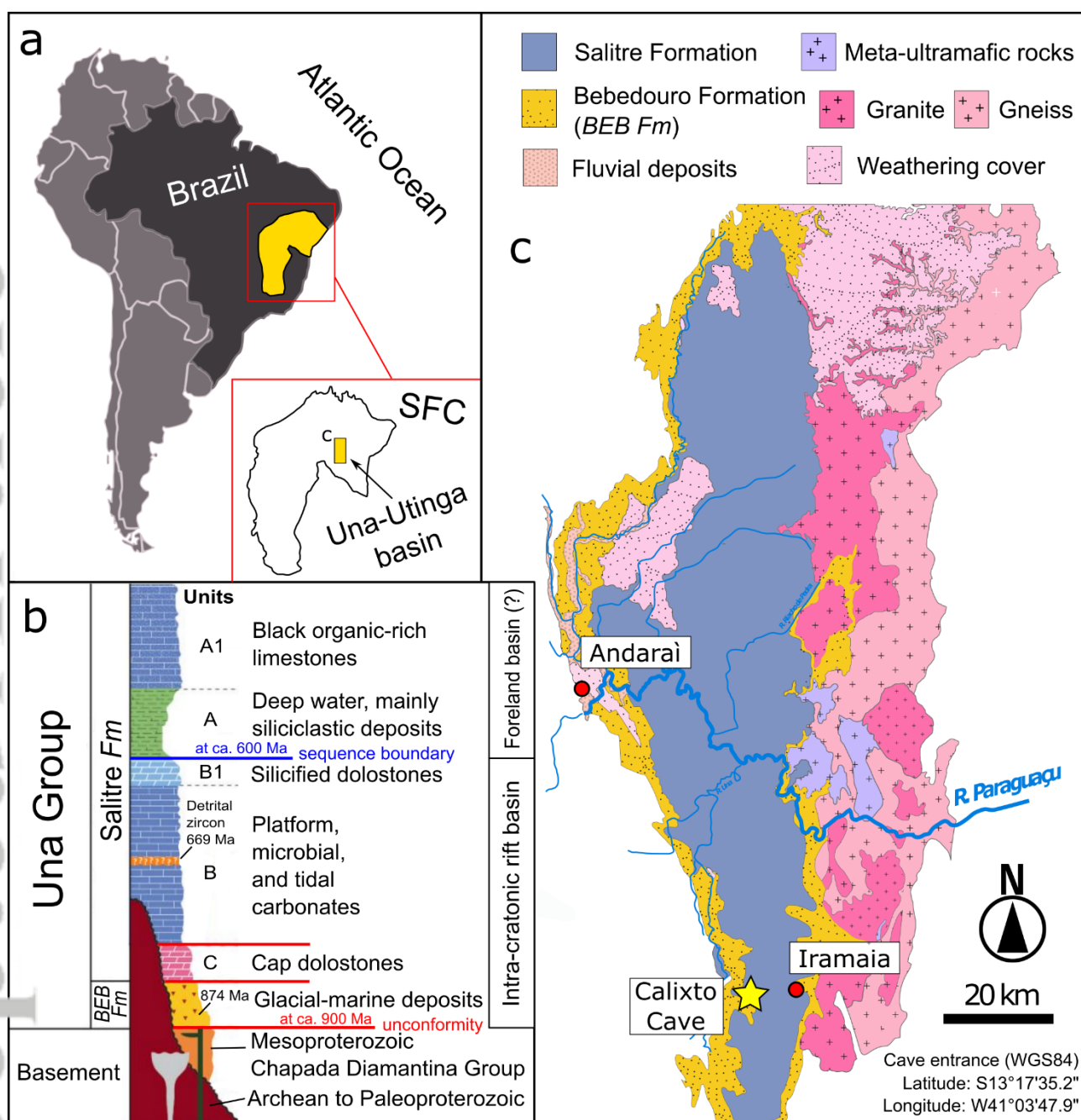


Figure 1. Geological setting: a) Location of the Una-Utinga basin in the São Francisco Craton (SFC) in northeastern Brazil; b) Conceptual stratigraphic column (not to scale) of the Una Group and the underlying basement rocks (modified from Misi et al., 2007 and Santana et al., 2021); c) Geological map of the Una-Utinga basin (Brazil), with the location of the Calixto Cave (modified from Pisani et al., 2022).

The Salitre Fm hosts hundreds of karst systems, some of which are among the longest known in South America (Auler, 2017). Most of these caves have a hypogene origin and were interpreted

as the result of hydrothermal alteration by rising acidic solutions migrating through the fractured basement (Klimchouk et al., 2016; Balsamo et al., 2020; Pontes et al., 2021).

Some caves in the São Francisco Craton are also associated with silicification (Bertotti et al., 2020; La Bruna et al., 2021; Souza et al., 2021) or contain hydrothermal minerals, e.g., quartz and chalcedony filling veins and vugs (Cazarin et al., 2019). Furthermore, in several sites of the Una-Utinga and Irecê basins, hydrothermal mineral assemblages of quartz, sphalerite, barite, and galena form Mississippi Valley Type (MVT) ore bodies (Kyle and Misi, 1997; Misi et al., 2012; Caird et al., 2017; Cazarin et al., 2021).

Among these caves, Calixto Cave represents a close analogue for karstified and silicified hydrocarbon reservoirs. The middle portion of the cave (middle storey; Fig. 2) is a sub-horizontal and stratigraphically confined network of conduits mostly developed within silicified dolostone layers with a SiO_2 content up to 80–85 wt.% (unit B1, Fig. 2b; Pisani et al., 2022). These silica-rich layers have a high permeability due to a combination of high fracture density and early-stage hypogene processes involving silica dissolution and precipitation (Pisani et al., 2022).

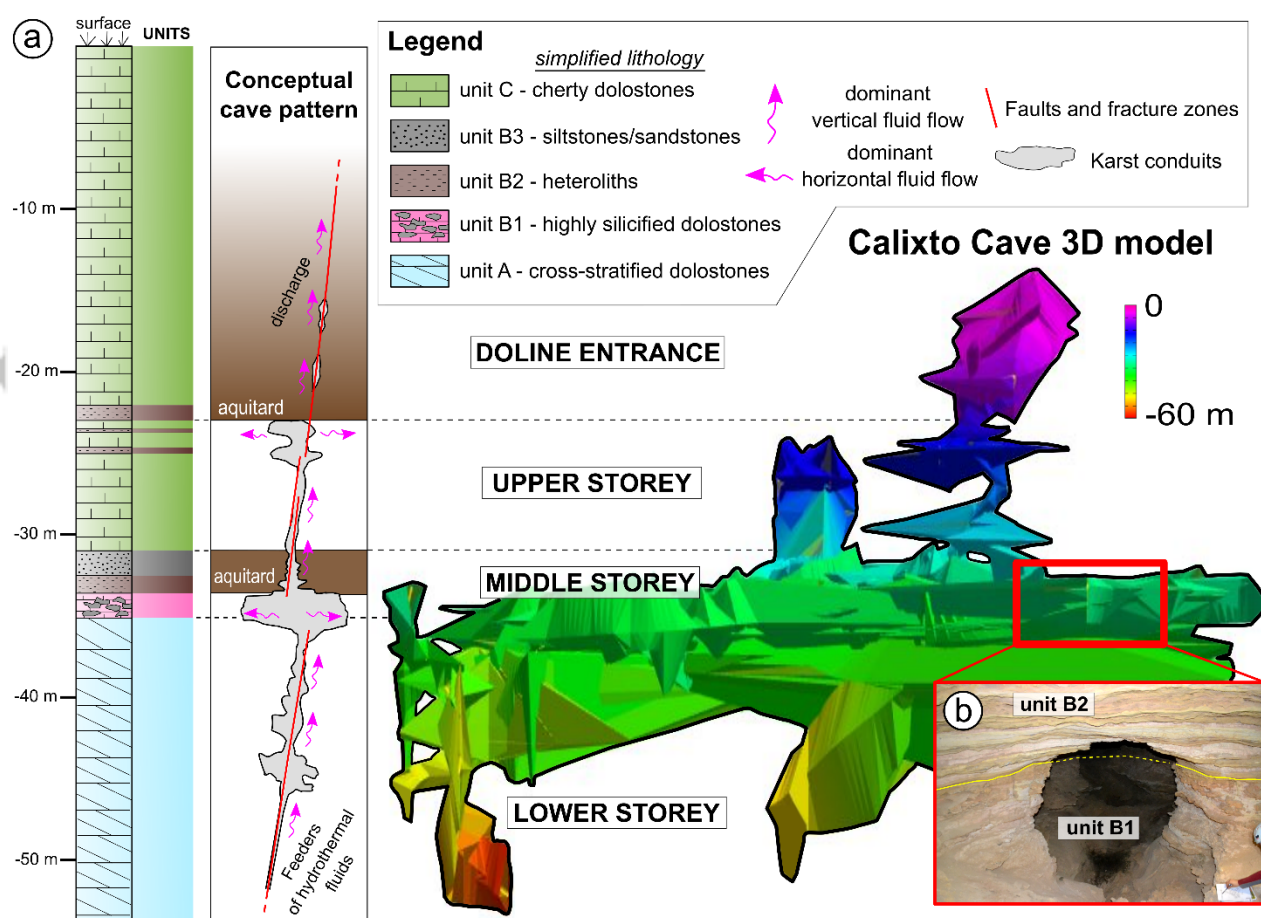


Figure 2. a) Lithostratigraphic log and schematic conceptual model of Calixto Cave conduit network. A 3D model of the cave is also shown (modified after Pisani et al., 2022). b) example of a master conduit in the middle storey, mostly localized in the sedimentary unit B1 (highly silicified dolostones).

3. Material and methods

To assess the origin of silica dissolution-precipitation processes in the Calixto Cave, we studied samples consisting of megaquartz (euhedral quartz crystals larger than 100 μm , generally up to 1-2 mm; Marin-Carbonne et al., 2014; Teboul et al., 2019), chalcedony, and chert (lithotype composed of microcrystalline quartz). Quartzite samples from the Chapada Diamantina Group (Fig. 1b) were analyzed for comparison.

3.1 Quartz and fluid inclusion petrography

Thirty-one thin sections were prepared and examined using a petrographic microscope to identify their main textural and petrographic characteristics. Five ca. 100 μm -thick doubly polished sections were prepared and examined for the presence of fluid-inclusion assemblages (FIAs) using a petrographic microscope. FIAs are defined as petrographically discriminated, cogenetic groups of fluid inclusions (Goldstein and Reynolds, 1994; Goldstein, 2003), which record the physical and chemical conditions of the fluid system at the time of trapping, assuming inclusions did not re-equilibrate (Bodnar, 2003). Roedder's criteria for FIAs classification according to the timing of entrapment were used (Roedder, 1984; Goldstein and Reynolds, 1994). FIAs were classed as primary (P), secondary (S), pseudosecondary (PS), or undetermined (U; no clear relationships with crystal growth could be established).

First-order features supporting the primary origin of FIAs are their occurrence in tridimensional clusters or their association with crystal growth zones. Different modes of occurrence of primary inclusions have been observed: FIAs associated with well-defined crystal growth zones (P1), isolated 3D clusters of inclusions of well-developed negative-crystal shapes (P2), or isolated 3D clusters of inclusions of elongated or irregular shapes (P3).

After identifying the main petrographic and textural characteristics of fluid inclusions, seven small fragments of the thick sections (up to 5 mm in diameter) were prepared for microthermometric measurements.

3.2 Fluid inclusion microthermometry

Microthermometric characteristics of fluid inclusions were determined using a Linkam THMS600 heating-freezing stage mounted on an Olympus BX41 microscope, using a 40x objective and a condenser lens at the University of Innsbruck. The stage was calibrated by using H₂O-CO₂ synthetic fluid inclusions. The accuracy of the calibration is ± 0.1 °C.

Homogenization temperatures (T_h) were determined on the FIAs by heating the samples from room temperature using the cycling technique described by Goldstein and Reynolds (1994). Freezing experiments were performed after measuring T_h . Inclusions were cooled to -180 °C and then slowly heated to detect the potential formation of solid phases (e.g., clathrates, salt hydrates, ice). Volume fractions of individual fluid inclusions (ratios of the vapor to liquid phases, V:L) were estimated visually at room temperature.

3.3 Fluid inclusion Raman spectrometry

The composition of representative individual inclusions was determined using Raman spectroscopy at room temperature and at cryogenic temperatures (Goldstein and Reynolds, 1994; Bodnar, 2003; Samson and Walker, 2000; Bakker, 2004; see Supplementary Materials for further details). Raman analyses were performed at the University of Innsbruck with a Horiba Jobin-Yvon Labram-HR800 spectrometer, equipped with a 532.18 nm laser and a Linkam THMS600 heating/freezing stage. Two to three accumulations were used during spectral acquisitions. Raman spectra were processed with LabSpec software (ver. 6.6.2.7). Calibration was performed using a standard Si-wafer with known reference Si-Si vibration at 520.7 cm^{-1} .

3.4 $\delta^{18}\text{O}$ and $\delta^{30}\text{Si}$ analyses

Oxygen ($\delta^{18}\text{O}$) and silicon ($\delta^{30}\text{Si}$) isotope values were analyzed using an in-situ secondary ion mass spectrometry (SIMS) technique (Abraham et al., 2011; Kleine et al., 2018) at the NordSIMS laboratory of the Swedish Museum of Natural History. Two individual grains for each silica sample (0.2 to 1 mm in size) were embedded in epoxy along with the quartz standard UNIL-Q1 (Seitz et al., 2016). The sample mounts were polished to $1\text{ }\mu\text{m}$ and gold coated.

Each grain was chemically characterized using a scanning electron microscope (SEM) Tescan Vega 3 LMU equipped with an energy dispersive spectroscopy (EDS) Apollo-X SDD detector at 20 kV accelerating voltage, 1.2 nA beam current, and 5–10 μm beam diameter, at the Earth Sciences Department of the University of Genova. EDS spectra and back scattered electron (BSE) images (see

Supplemental Materials) were acquired to identify the most suitable locations (e.g., almost pure SiO₂ phase) for in-situ isotope analyses. One to two analyses for each SiO₂ grain were performed for silicon and oxygen isotopes.

The isotope values are reported relative to V-SMOW and NBS28 using the standard delta notation. Errors associated with the stable isotopes data range between $\pm 0.13\text{‰}$ and $\pm 0.20\text{‰}$ for $\delta^{30}\text{Si}$, and from $\pm 0.19\text{‰}$ to $\pm 0.38\text{‰}$ for $\delta^{18}\text{O}$.

Geochemical modelling of $\delta^{30}\text{Si}$ and $\delta^{18}\text{O}$ isotope systematics was carried out assuming an open system-type Rayleigh model for the simulation of quartz precipitation in result of cooling/boiling hydrothermal fluids, burial diagenesis at different temperatures, and fluid mixing. Rayleigh distillation curves were calculated following the procedure of Kleine et al. (2018). Further details on the adopted calculations and reference equations are reported in the Supplementary Materials.

3.5 U-Th-Pb dating

Quantitative analyses of selected monazite grains were performed at the University of Graz using a JEOL JXA-8530F Plus electron microprobe equipped with five wavelength-dispersive spectrometers (radius of the Rowland circle = 140 mm). Operating conditions were 15 kV accelerating voltage, 150 nA beam current and 1 μm beam diameter. The X-ray lines, counting times, calibration materials, and interference corrections are listed in the Supplementary Material Table S1, together with the data for monazite reference materials measured to assess the accuracy of Th-U-total Pb dates. Matrix correction follows the method of Bence and Albee (1968) with α -factors after Kato (2005). The full data on monazite analyses are presented in the Supplementary Materials (Table S2).

4. Results

4.1 Petrographic observations

Silica deposits studied in thin and thick sections were classified based on their petrographic and textural characteristics in five facies, defined as micro-crystalline quartz (qtz-mc), chalcedony and “jigsaw” mosaic quartz (qtz-C), early-stage megaquartz (qtz-I), late-stage megaquartz (qtz-II), and quartz-rich hydraulic breccias (qtz-br).

Qtz-mc replaces the precursor dolomite forming silicified zones, where the main sub-horizontal conduits of the cave are concentrated (Fig. 2; middle storey; Pisani et al., 2022). Qtz-mc is organized in nodules and bands (namely chert) sometimes hosting patches of residual dolomite

(Fig. 3). The latter shows a grain size of 5-40 μm , with predominantly sub-euhedral crystal structures. Enlarged fractures, solutional vugs and cavernous voids up to a several millimeters in size (classified as meso-pores in the range of 4-32 mm, based on the definition by Choquette and Pray, 1970) are common in these silicified rocks observed at the thin-section scale. Occasionally, larger irregular mega-pores are observed at the hand sample scale, reaching up to 4-5 cm in their larger axes. Examples of representative vugs, cavernous voids and corrosion features in the cherts are shown in the Supplementary Materials (Fig. S1).

Small crystals (< 10-20 μm) of Fe- and Fe-Ti oxides (less commonly, pyrite) are associated with qtz-mc. Fe hydroxides occur primarily as overgrowths of Fe oxides and sulfides or pseudomorphs after them.

Qtz-C consists of chalcedony (Fig. 3b) or “jigsaw” mosaic quartz (Moncada et al., 2012) filling micro-veins and solutional vugs in the chert nodules and at the transition zone with megaquartz crystals (Figs. 3c, 3d). Sometimes, qtz-C is found in the core of the larger quartz crystals (Fig. 4c). The transition between qtz-C and qtz-I is usually gradual and diffuse (Fig. 5). Chalcedony fibers are typically aligned in a parallel or spherulitic fashion and have a “feathery” appearance.

Qtz-I consists of megaquartz crystals with cloudy cores and colloform-plumose textures (Sander and Black, 1988; Saunders, 1994; Moncada et al., 2012; Figs. 4a, 4b, 5a, 5b). Such textures commonly occur in the inner zones of qtz-I crystals (Fig. 5b).

The second facies of megaquartz (qtz-II) represents the final episode of crystallization in the paragenetic sequence (Fig. 5a). It shows zonal or massive textures and a large crystal size variability (0.2 to 5 mm; Figs. 4c, 4d, 5c, 5d). Both qtz-I and qtz-II show undulose extinction, deformation lamellae, and recrystallization textures like interfingering subgrain boundaries (Passchier and Trouw, 2005), indicating crystal lattice deformation acquired at depth (Figs. 4e, 4f).

Another type of quartz mineralization found in the Calixto Cave is qtz-br, which consists of subhedral or anhedral quartz fragments with breccia-like textures (Fig. 5e), usually associated with abundant K-feldspar with sericitic alteration. This facies is commonly found along bedding interfaces and lamination of the heterolith layers overlying the main cave passages in the middle and upper storeys (Fig. 2). Brecciation is represented by angular clasts of silica and K-feldspar in a matrix of fine-grained detrital grains with heterolithic composition. Alteration halos rich in muscovite and altered K-feldspar are common in the matrix associated with the brecciated textures, spanning from hundreds of μm to a few mm around the quartz-rich zones (Pisani et al., 2022). Besides K-feldspar

and muscovite, the halos host disseminated sulfides, Fe oxides, and Fe hydroxide stains (up to 200–250 μm in size) and monazite grains (Pisani et al., 2022).

Solid inclusions (ca. 5–50 μm in size) of anhydrite, barite, K-feldspar, muscovite, sulfides, Fe-Ti oxides, and apatite (Pisani et al., 2022) are abundant in early qtz-I and often found in qtz-C and qtz-br.

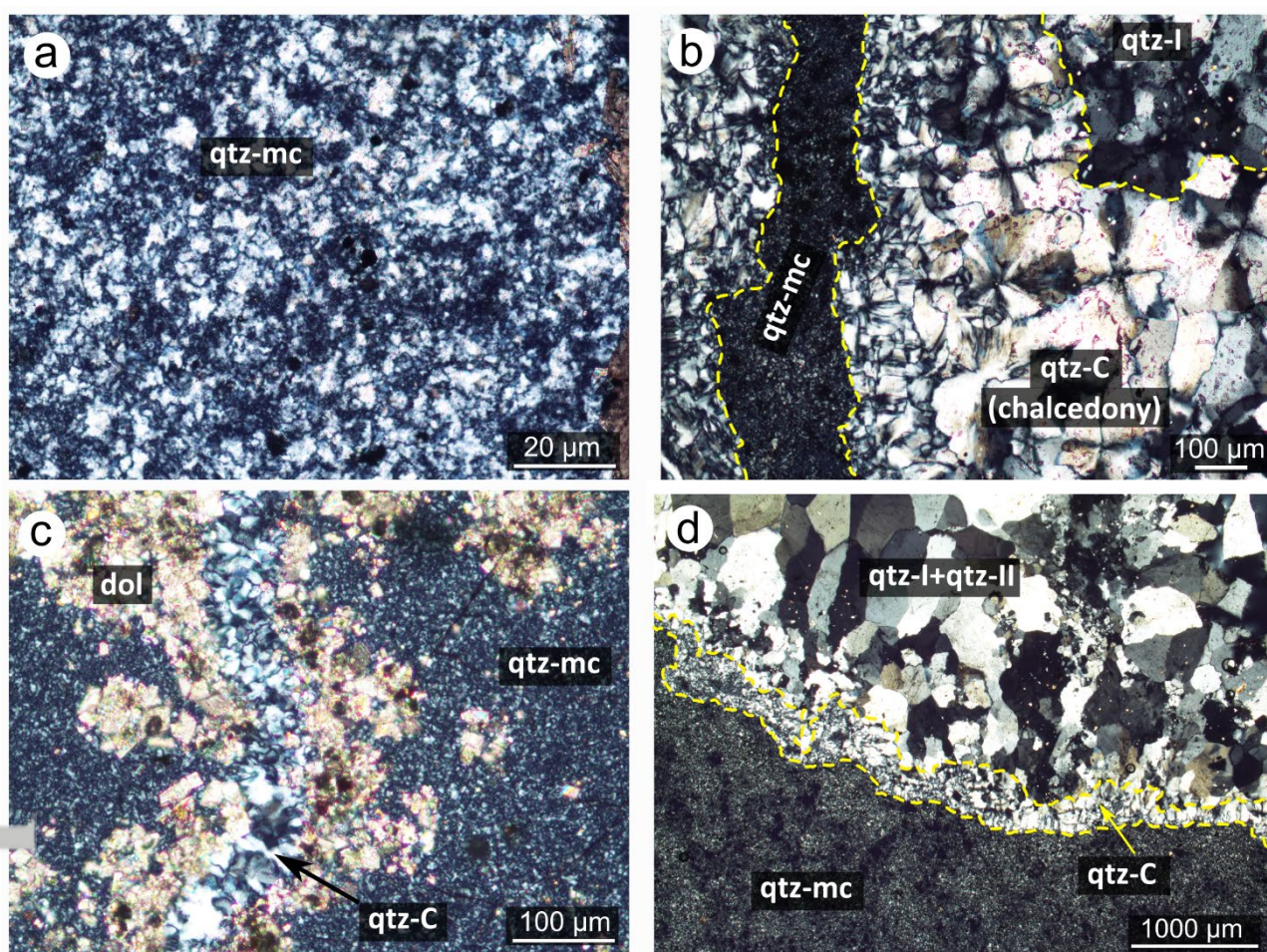


Figure 3. a) Microcrystalline quartz (qtz-mc) replacing the original dolomite and forming chert nodules. b) Qtz-mc, chalcedony (qtz-C), and early stage megaquartz (qtz-I) in the upper right corner. c) Residual dolomite (dol), qtz-mc and jigsaw quartz (qtz-C). d) Transition between qtz-mc and a solutional macro-pore in it, lined with qtz-C, qtz-I and qtz-II. Photographs at cross-polarized light. The yellow dashed lines mark the transition between silica facies.

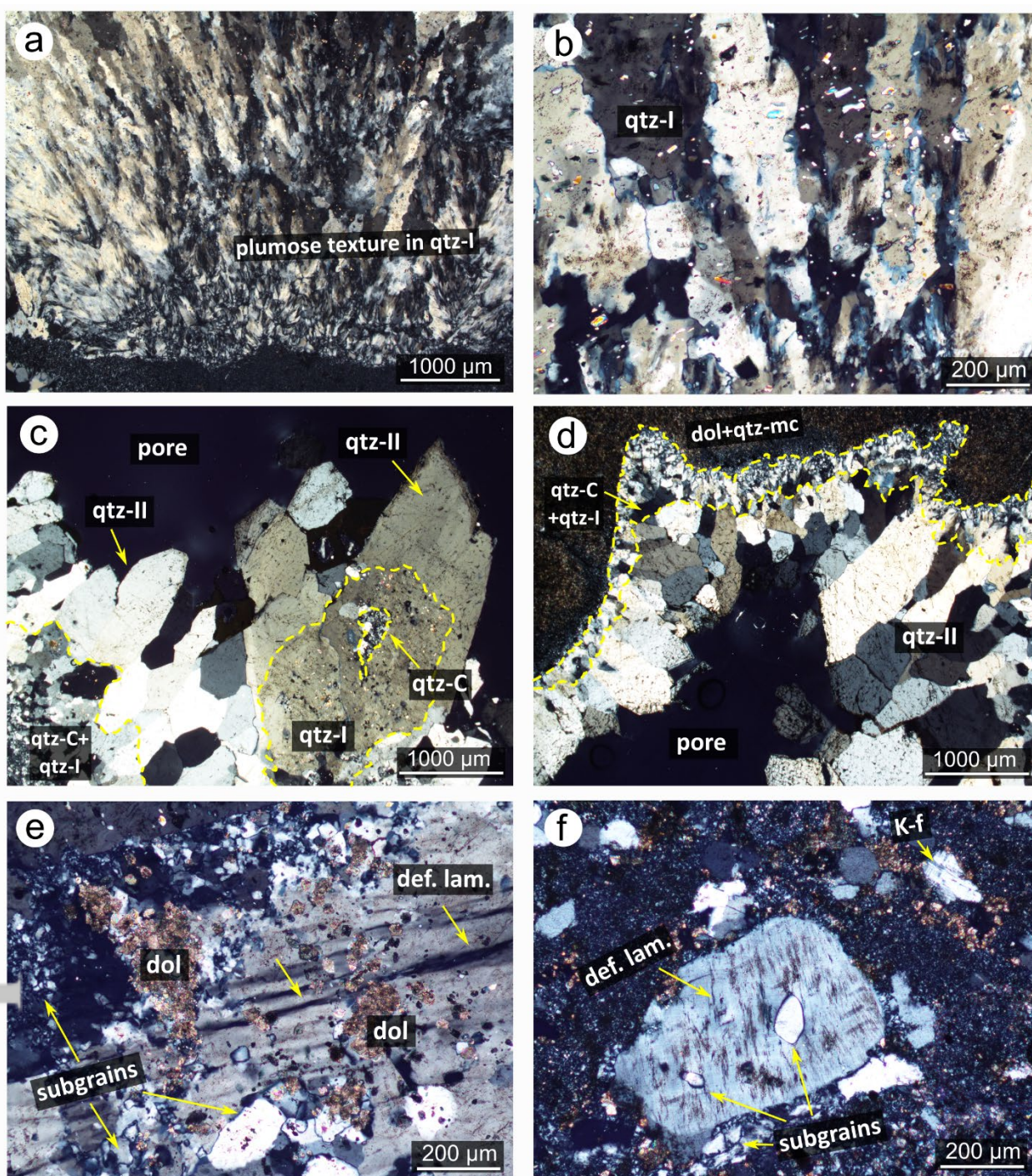


Figure 4. a) Megaquartz with plumose texture (qtz-I). b) Mineral inclusions with high interference colors (mostly anhydrite, barite and muscovite) in early-stage megaquartz (qtz-I). c) Late-stage megaquartz crystals (qtz-II) partially filling a solutional macro-pore. Note cores composed of qtz-C and qtz-I in a large qtz-II crystal. d) Residual dolomite partially replaced by silica (dol+qtz-mc), and the paragenetic sequence comprising qtz-C, qtz-I, and qtz-II filling a solutional macro-pore. e-f) Deformation lamellae (def. lam.) and recrystallized subgrains in qtz-II. Photographs at cross-polarized light. K-f = K-feldspar; dol = dolomite. The yellow dashed lines mark the transition between silica facies.

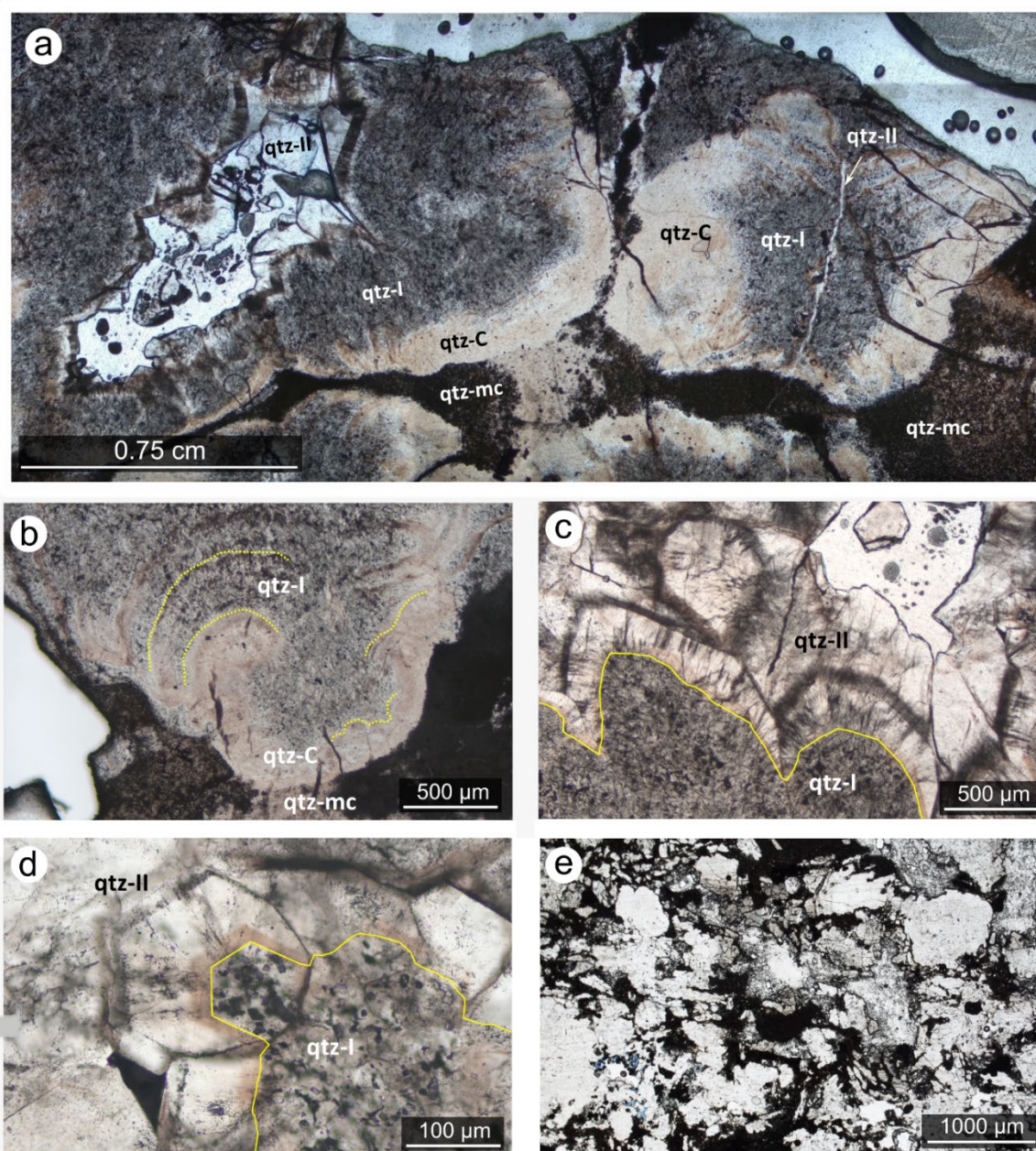


Figure 5. a) Paragenetic sequence of quartz facies from chert (qtz-mc) to (in order of growth) qtz-C (chalcedony), qtz-I (colloform-plumose quartz with cloudy cores), and qtz-II (massive or zonal euhedral megaquartz crystals). b) Contact between qtz-mc and qtz-C/qtz-I facies. Yellow dotted lines highlight colloform quartz bands. c) Qtz-I showing cloudy cores with randomly distributed inclusions, followed by qtz-II showing well-developed growth zones rich in primary fluid inclusions. Yellow solid lines highlight the transition between qtz-I and qtz-II. d) Detail of a qtz-I/qtz-II transition followed by defined growth zones parallel to crystal boundaries. Yellow solid lines highlight the transition between qtz-I and qtz-II. e) Breccia microtexture (qtz-br) in a heterolith layer, with fragmented clasts of silica and K-feldspar surrounded by a matrix of fine-grained detrital clasts.

4.2 Fluid inclusion petrography

Most of the fluid inclusions were found in qtz-I and qtz-II facies (Figs. 5, 6). Qtz-I possess cloudy cores (Fig. 5a) whose cloudy appearance is due to abundant mineral inclusions, randomly distributed two-phase liquid-vapor (L+V) inclusions ($< 10\ \mu\text{m}$ in size) with inconsistent V:L ratios (Fig. 6e), and dark large monophasic (V) inclusions with shapes approaching negative-crystal (e.g., inclusions with surfaces resembling crystal faces; Goldstein and Reynolds, 1994) (Fig. 6f).

The transition between qtz-I and qtz-II usually features well-developed growth zones with trails of primary two-phase L+V inclusions (Figs. 5c, 5d, 6a). In qtz-II, growth zones with trails of primary two-phase FIAs are common (Figs. 6a, 6b). Inclusions in these FIAs have sizes of $5\text{--}10\ \mu\text{m}$ and show visually consistent V:L ratios (0.10–0.15). Other primary FIAs are associated with 3D clusters of large intracrystalline inclusions (up to $10\text{--}15\ \mu\text{m}$ in size), often having negative-crystal shapes (Fig. 6c). The boundaries between the quartz crystals commonly host irregular and imperfectly healed microfractures. Occasionally, dark single-phase (V) inclusions were observed in this type of quartz; no compelling evidence of their primary origin was recognized.

The qtz-mc and qtz-C facies show no recognizable FIAs due to the small size of the crystals. Abundant negative-crystal shaped microcavities (ghosts of rhombohedral dolomite grains; Fig. 6d) and relicts of the pristine dolostone rock are present (Fig. 4d).

The qtz-br facies shows the coexistence of 3D clusters of large intracrystalline L+V inclusions (up to $20\ \mu\text{m}$ in size) with consistent V:L ratios (0.10–0.15) and solid inclusions. Irregular-shaped dark single-phase (V) inclusions are also present in this facies.

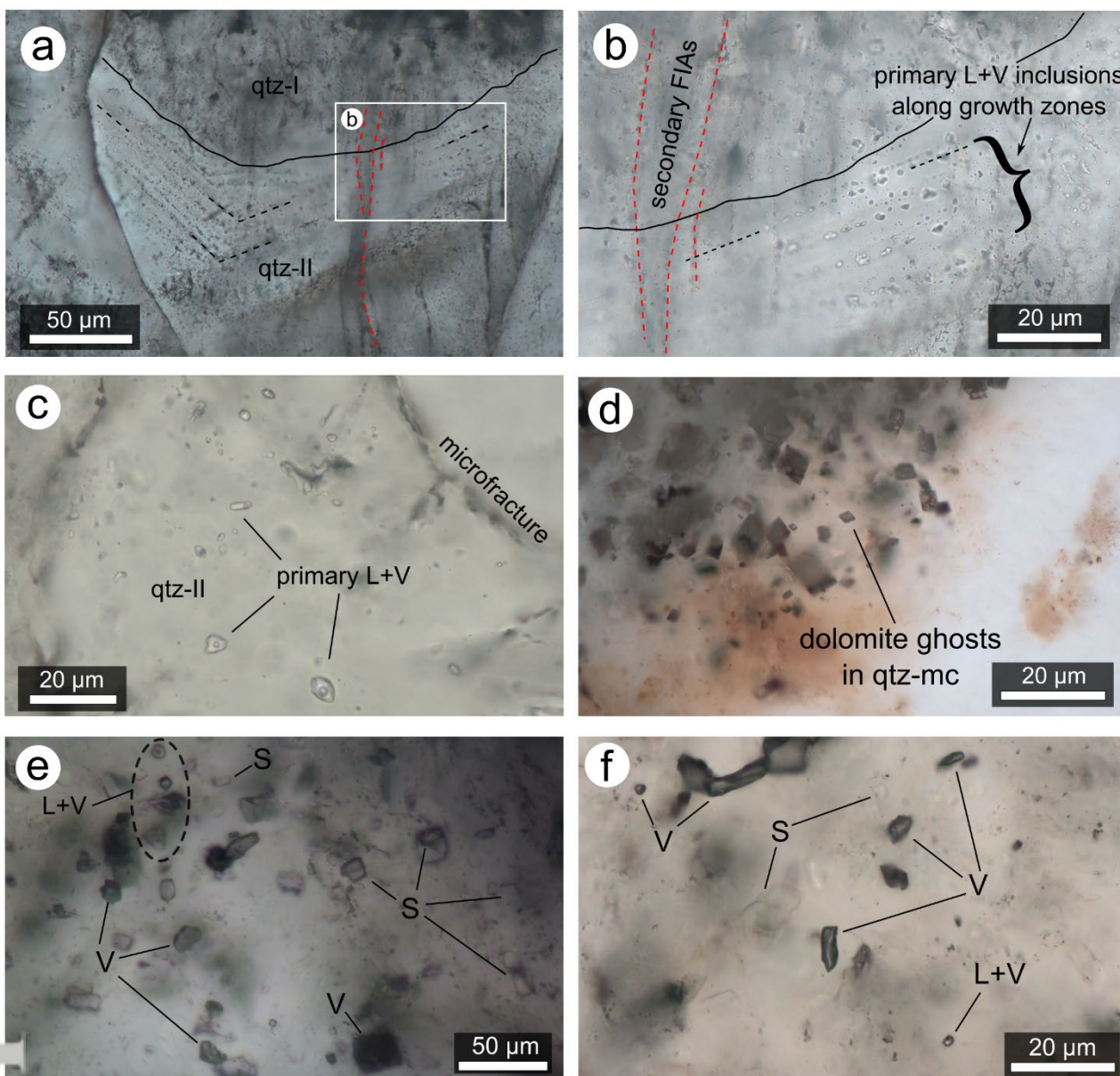


Figure 6. a) Trails of primary fluid inclusions (highlighted with black dashed lines) aligned parallel to qtz-II crystal faces. Black solid line marks the transition between qtz-I (cloudy core) and qtz-II (megaquartz with zonal texture). b) Close-up of inset in 'a': Primary two-phase (L+V) inclusions and trails of secondary inclusions, cross-cutting the primary FIAs (highlighted with red dashed lines). c) 3D cluster of primary fluid inclusions in qtz-II. Most of the inclusions have negative-crystal shapes. d) Rhombohedral dark cavities (ghosts of dolomite grains) in the qtz-mc facies. e-f) Coexisting two-phase (L+V), single-phase (V) fluid and solid (S) inclusions in the cloudy cores of qtz-I.

4.3 Fluid inclusion microthermometry

Four selected samples of qtz-II and one sample of qtz-br were studied to obtain microthermometric data from 57 FIAs (236 individual inclusions). The only phase transition

observed during the heating runs was homogenization, which always occurred in the liquid phase. For most of the primary FIAs, T_h was consistent (according to the criteria of Goldstein and Reynolds, 1994). Fig. 7a shows the cumulative frequency histogram of the entire dataset ($n=210$) without three FIAs showing inconsistent T_h data (see Figs. S2 and S3 in the Supplementary Materials for the whole dataset). About 95% of the primary FIAs homogenize in the 175–210 °C interval. The bimodal distribution has two well-defined peaks centered at 185 °C and 200 °C.

After the heating runs, freezing measurements were used to assess the salt composition of representative FIAs. Due to the very small size of most of the inclusions, phase changes during cooling runs were recognized only in a limited subset of FIAs ($n=62$; Fig. 7b). The two-phase aqueous inclusions were completely frozen (dark or brownish mosaic of crystals) at around –70° to –60 °C. During slow heating, several phase transitions were observed between –60 °C and room temperature. Most inclusions showed a clear first melting between –52 °C and –47 °C. With progressive heating, an intermediate melting temperature between –28 °C and –26 °C was observed in most of the FIAs with the sudden disappearance of the darkish, granular solid phase (likely small hydrohalite crystals), leaving the inclusions with only rounded and larger crystals, liquid, and vapor phases. The final melting of the last solid phase (T_m) occurred between –26 °C and –15 °C. About 90% of the primary inclusions have T_m values between –25 °C and –20 °C (median at –23 °C).

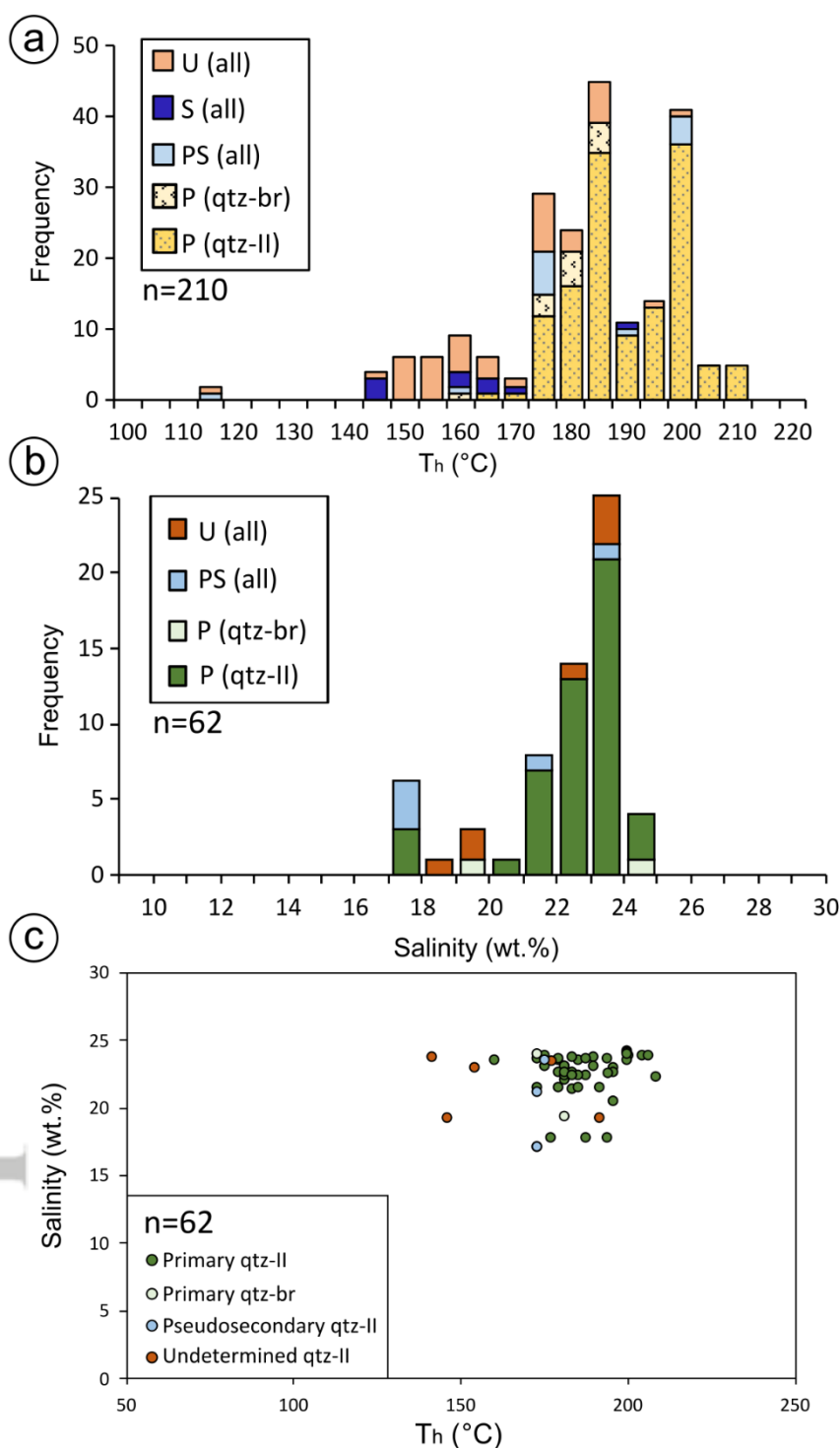


Figure 7. a) Frequency histogram of the homogenization temperatures (T_h) for the whole dataset ($n=210$), excluding three FIAs ($n=26$) that showed inconsistent results (according to the criteria of Goldstein and Reynolds, 1994). Undetermined (U), pseudo-secondary (PS) and secondary (S) assemblages are plotted in single groups, while quartz facies differentiate primary (P) assemblages. b) Frequency histogram of estimated salinity (NaCl-CaCl₂-equivalent) for all FIAs studied at low

temperature ($n=62$). c) T_h -salinity plot for the fluid inclusions where both T_h and salinity data were acquired ($n=62$).

4.4. Raman spectrometry of fluid inclusions

As no gases were determined during microthermometry (e.g., melting of a carbonic-phase or clathrate formation during the freezing experiments), Raman spectroscopy analyses were performed on a set of representative FIAs (samples 1094A-5, 1094B-3). Aqueous fluid inclusions hosted in qtz-I, qtz-II and qtz-br show a very broad peak at the characteristic wavenumbers of liquid H_2O (ca. 3400–3500 cm^{-1}), and occasional peak at the wavenumber characteristic of HCO_3^- solute (1017 cm^{-1}). These peaks were determined as weak in all spectra; no other gas phases (e.g., CO_2 , H_2S , SO_2 , CH_4) were detected. Such spectroscopic determinations are consistent with the lack of microthermometric evidence of a carbonic-phase or clathrate formation during the freezing experiments (Dubessy et al., 2001; Marchesini et al., 2019).

Raman spectra were also acquired at $-170\text{ }^{\circ}C$, $-100\text{ }^{\circ}C$, as well as at any observed phase transitions to detect the presence of ice, hydrohalite and salts in the spectral range of 2700 to 3550 cm^{-1} (Samson and Walker, 2000; Bakker, 2004; Baumgartner and Bakker, 2010). Most of the frozen inclusions showed Raman spectra with poorly defined peaks. However, few representative primary inclusions that were analyzed during progressive heating present broad peaks indicating the presence of a mixture of ice, NaCl hydrate (hydrohalite), and $CaCl_2$ hexahydrate (antarcticite). These solid phase peaks disappeared from the Raman spectra at the observed melting temperatures, as expected by the phase behavior typical of the H_2O -NaCl- $CaCl_2$ system at low temperatures (see Supplementary Materials for further details).

4.5 Oxygen and Silicon isotopes

The results of oxygen and silicon stable isotope analyses for Calixto Cave samples ($n=26$) and quartzites from the Chapada Diamantina basement ($n=4$) are summarized in Fig. 8 and Table 1. The $\delta^{30}Si$ values of the Calixto Cave samples range from -3.6 to 2.6‰ , while the Chapada Diamantina basement quartzites have $\delta^{30}Si$ values of 0.1 to 0.4‰ (Fig. 8a). The $\delta^{18}O$ values of the cave samples range between 22.1 and 29.7‰ , whereas those from the basement quartzites cluster around 13‰ (Fig. 8b).

The $\delta^{30}Si$ values of cherts found in Calixto Cave define a general trend toward more negative values going from the “pristine” or scarcely corroded cherts (0.9 to 1.5‰) to the highly corroded

ones (−2.6 to −3.6‰) (Fig. 8c). This trend is associated with an increase in the $\delta^{18}\text{O}$ values (by up to 7‰).

Diagnostic textural features of the early stage megaquartz (qtz-I) and qtz-C were hardly distinguishable in SEM observations. Therefore, they were classified into a single group. Samples from the middle storey megaquartz and chalcedony deposits have heterogeneous values (Figs. 8a, 8b), with the $\delta^{30}\text{Si}$ between −1.9 and 2.6‰, and the $\delta^{18}\text{O}$ between 23.9 and 29.7‰.

Table 1. $\delta^{30}\text{Si}$ and $\delta^{18}\text{O}$ isotope results with associated uncertainties (1σ).

Locality	Sample ID	Silica facies	Grain ID	$\delta^{30}\text{Si}$ (‰ NBS28)		$\delta^{18}\text{O}$ (‰ V-SMOW)	
Chapada Diamantina basement	CARB-1040	quartzite bedrock	16A	0.15	±0.17	13.58	±0.20
			16A-b1	0.12	±0.18	13.71	±0.19
			16B	0.30	±0.17	13.68	±0.18
			16B-b2	0.40	±0.19	13.73	±0.18
Calixto Cave	CARB-1081	qtz-I/chalcedony	19A	1.06	±0.17	24.95	±0.19
			19B	-0.52	±0.17	29.27	±0.20
	CARB-1063A	corroded chert	20A	0.95	±0.17	23.75	±0.20
			20B	-1.57	±0.20	24.18	±0.20
	CARB-1063B	qtz-I/chalcedony	21A	0.86	±0.18	26.05	±0.20
			21B	-0.12	±0.18	28.49	±0.19
	CARB-1098	chert	22A	0.98	±0.17	24.36	±0.27
			22A-b1	0.93	±0.14	23.47	±0.36
			22B	1.12	±0.20	23.56	±0.32
			22B-b2	1.07	±0.13	23.99	±0.38
	CARB-1085	chert	23A	1.48	±0.17	22.10	±0.36
			23B	0.88	±0.20	22.42	±0.36
	CARB-1094B	qtz-II	25A	-1.90	±0.18	23.95	±0.19
		corroded chert	25B	0.84	±0.19	23.55	±0.19
	CARB-1094D	corroded chert	27A	0.49	±0.17	25.70	±0.36
			27B	0.65	±0.17	24.43	±0.37
	CARB-1094E	corroded chert	28A	-0.19	±0.20	24.14	±0.21
			28B	-1.09	±0.17	24.19	±0.19
	CARB-1094F	qtz-I/chalcedony	29B	-0.83	±0.17	29.72	±0.19
		qtz-II	29A	-1.40	±0.18	25.30	±0.20
	CARB-1094G	qtz-II	30A	-1.17	±0.17	26.84	±0.36
			30B	2.60	±0.17	28.41	±0.36
	CARB-1094H	highly corroded chert	31A	-2.98	±0.17	28.66	±0.36
			31A-b1	-2.63	±0.20	27.95	±0.38
			31B	-3.64	±0.17	28.29	±0.38
			31B-b2	-3.30	±0.18	25.98	±0.36

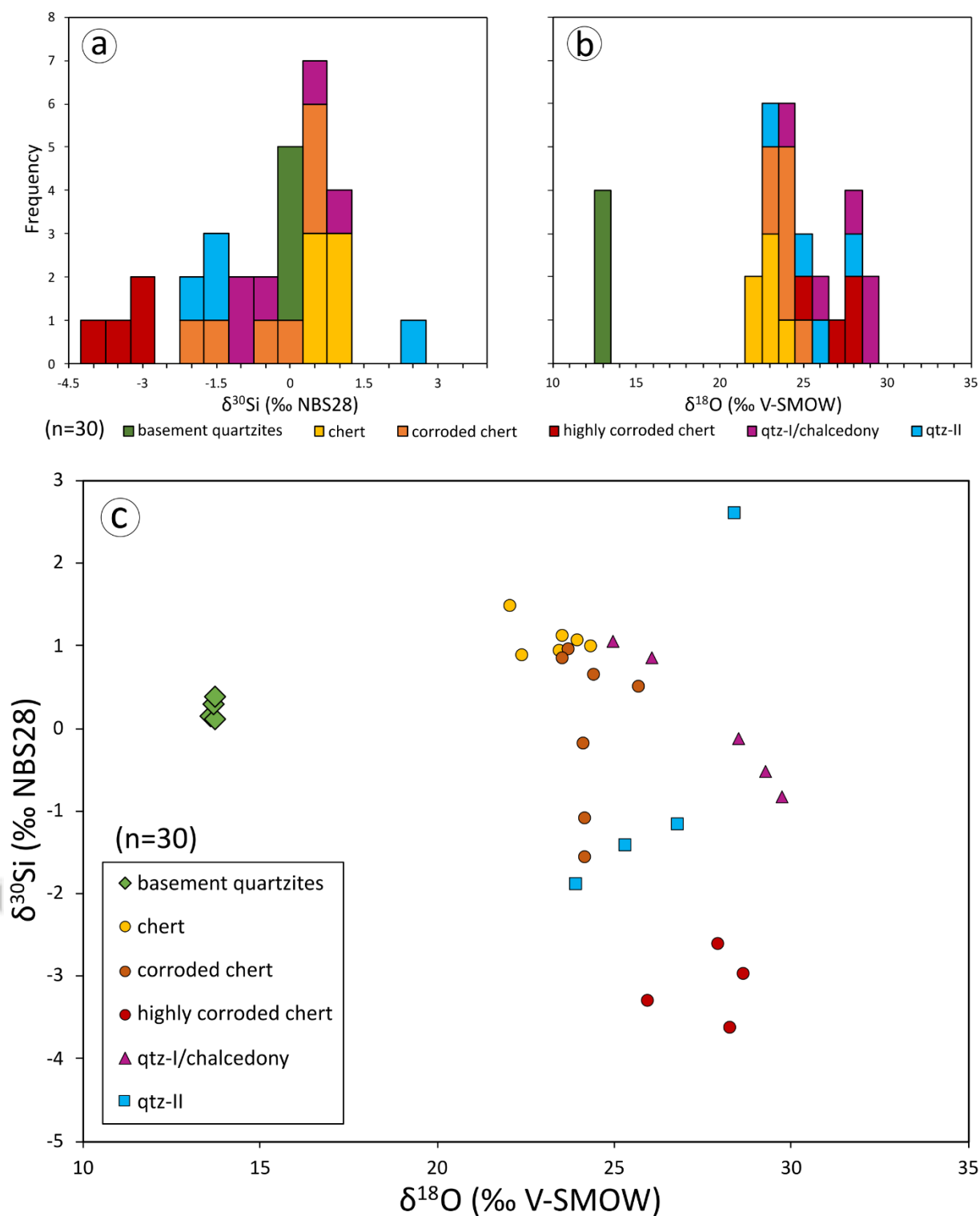


Figure 8. a) Frequency histogram of $\delta^{30}\text{Si}$ data of silica samples from Calixto Cave and Chapada Diamantina basement quartzites. b) Frequency histogram of $\delta^{18}\text{O}$ data of the silica samples from Calixto Cave and Chapada Diamantina basement quartzites. c) The $\delta^{18}\text{O}$ - $\delta^{30}\text{Si}$ data.

4.6 Monazite geochronology

Thirty-two U-Th-Pb analyses were performed on fourteen monazite grains (Table 2, Fig. 9). All grains were smaller than ca. 10 μm , had highly irregular shapes and were commonly crosscut by cracks and microfractures. The Th-U-total Pb dates range from ca. 2550 to 0 (Pb content below detection limit) Ma and four different groups were distinguished. The first and youngest group (group 1 in Table 2) is represented by 3 analyses of the same grain (siteD3-Mnz2) that cluster at 626 ± 17 Ma and have intermediate Y contents ($\text{Y}_2\text{O}_3=1.25$ wt.%). A second group comprising five analyses (group 2 in Table 2) of Y- and mostly Th-U-poor grains ($\text{Y}_2\text{O}_3=0.51$ wt.%) yielded dates between 1700 and 1100 Ma. The dominant and oldest group (group 3 in Table 2) at ca. 2000 Ma (one spot at 2500, twelve between 2200–1900 Ma) is relatively rich in Y (average $\text{Y}_2\text{O}_3=1.89$ wt.%), Th ($\text{ThO}_2=6.37$ wt.%), and Ca ($\text{CaO}=0.85$ wt.%). The last group of analyses (not shown in Table 2 and Fig. 9) comprises Y- and Th-U-poor analyses ($\text{Y}_2\text{O}_3<0.10$ wt.%; $\text{ThO}_2<1.65$ wt.%; U below detection limit) with Pb below the detection limit (around ca. 150 ppm; Montel et al., 1996). No reliable dates were calculated for this group.

Table 2. Th-U-total Pb dates obtained from electron microprobe dating of monazite.

ID site	number of analyses per site	calculated date (Ma)	2 σ (Ma)	group
SiteD3-Mnz2	3	644	26	1
		604	34	
		619	31	
SiteA-Mnz1	2	1716 (1402)	3 (7)	2
SiteC-Mnz1	1	1186	46	
SiteMatrix4	2	1526 1508	32 82	
SiteA-Mnz2	2	2554 2188	5 6	3
SiteA-Mnz3	2	1973	5	
		1983	5	
SiteMatrix1	2	2006	20	
		1933	20	
SiteMatrix4	1	1942	30	
SiteMatrix3	6	2005	4	
		1994	4	
		1982	4	
		2010	4	
		2006	4	
		1962	5	

Footnote: (Date in brackets)=analysis with a low total.

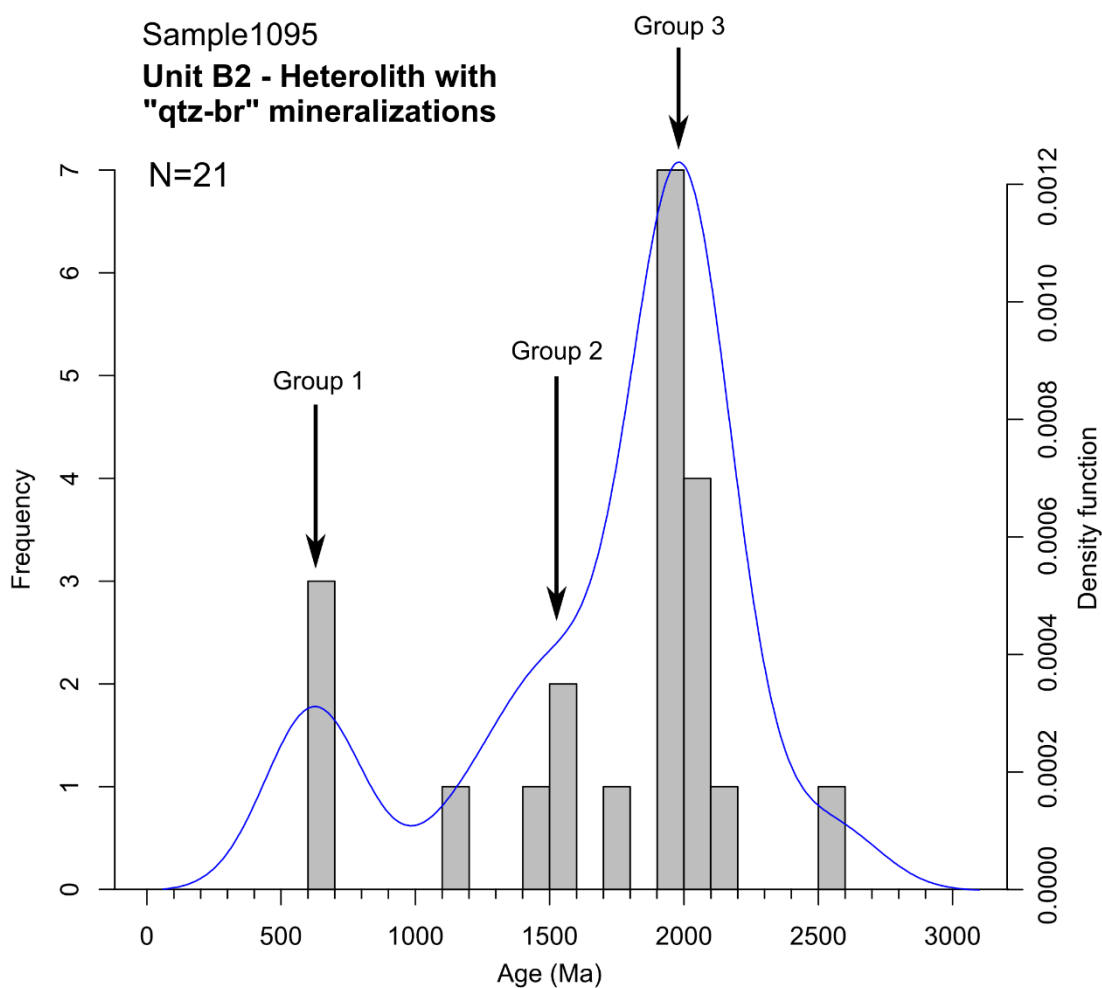


Figure 9. Frequency histogram and probability density distribution of the Th-U-total Pb dates for monazite grains in the heterolith unit with qtz-br mineralization (cf. Fig.2, unit B2).

5. Discussion

Hypogene caves and solutional karst porosity found in the carbonates of the Salitre Fm (Klimchouk et al., 2016; Cazarin et al., 2019; Bertotti et al., 2020; Pisani et al., 2022) and the nearby Chapada Diamantina Group (La Bruna et al., 2021; Souza et al., 2021) are often associated with silicified layers or hydrothermal mineralization containing quartz.

Silicification of marine carbonates is commonly the result of diagenetic processes (Maliva and Siever, 1989). The most representative silica crystallization sequence associated with increasing temperature during diagenesis is: 1) amorphous silica or opal-A; 2) cristobalite-tridymite (CT) opal; 3) microcrystalline quartz; 4) chalcedony; and 5) megaquartz (Maliva and Siever, 1989; Sander and Black, 1988; Marin, 2009; Marin-Carbonne et al., 2014). This sequence is often observed in marine carbonates, where calcite/dolomite grains are replaced by opal or microcrystalline quartz (e.g.,

forming chert nodules). The other quartz textures occur preferentially in large voids and open fractures (Hesse, 1989), representing either late-stage silica deposition at elevated temperature or recrystallization of micro-quartz/chalcedony.

It is important to note that the behavior of silica during the diagenetic evolution of carbonate sediments is more complex than the simple paragenetic sequence listed above. Various sediment-water interactions may act as either silica sinks or sources, for example: biodegradation of organic matter (Bennett et al., 1988), transformation of clay minerals, devitrification of volcanic ash (Siever, 1962; Siever and Woodford, 1973), or circulation of hydrothermal fluids (Wei et al., 2021). Chert with a predominantly volcanic silica source is recognizable by its high alkali, Al, and Ti contents, ghosts of volcanic glass shards, and associated volcanoclastic sediments (Pollock, 1987; Maliva and Siever, 1989). Another source could be direct precipitation from silica-rich seawater (Maliva and Siever, 1989; Ledevin et al., 2019), which could be expected for ancient Precambrian basins (Marin-Carbonne et al., 2014).

Based on the petrographic, textural, and stratigraphic evidence from Calixto Cave (Pisani et al., 2022 and this study) and the entire São Francisco Craton (Kyle and Misi, 1997; Klimchouk et al., 2016; Cazarin et al., 2019; Bertotti et al., 2020; La Bruna et al., 2021; Souza et al., 2021), two main sources may be invoked to explain the widespread silica precipitation associated with karst development in the study area: i) Si-enriched hydrothermal solutions rising through the fractured basement; and ii) Neoproterozoic connate (pore)water during burial diagenesis. Based on petrographic, mineralogical and speleogenetic observations, most of the works cited above interpreted silicification and karst development in the São Francisco Craton as a product of hydrothermal (hypogene) fluid circulation, even though no analytical data on quartz (e.g., stable isotopes, fluid inclusions, trace element composition) were reported so far.

In the following sections, the possible sources of silicification and silica dissolution-precipitation in Calixto Cave are discussed in the framework of the diagenetic evolution of the sequence.

5.1 Petrographic and microthermometric characteristics of silica

Like many Precambrian cherts (Maliva et al., 2005; Marin-Carbonne et al., 2014), no evidence of amorphous silica, opal-A, or opal-CT precipitated via biotic processes was found in the Calixto Cave sequence. The petrographic and textural characteristics of the chert nodules indicate that the first episodes of silica precipitation involved the replacement of the precursor carbonate with

microcrystalline quartz. This process was likely related to early diagenetic (shallow burial) conditions, as supported by the ubiquitous cross-cutting relations between cherts and all tectonic and diagenetic features (like burial-related fractures and bedding-parallel stylolites) found in the cave, as described by Pisani et al. (2022). Furthermore, evidence of intense dissolution prevails in the qtz-mc facies, with cavernous vugs, solution-enlarged fractures, and pores lined by qtz-C followed by megaquartz. Undulose extinction and deformation lamellae in megaquartz crystals also suggest that these crystals were subject to deformation after their deposition (Figs. 4e, 4f).

Megaquartz and chalcedony in marine carbonate sequences are usually products of silica recrystallization and cementation in a deep-burial setting or due to later hydrothermal/metamorphic processes (Marin-Carbonne et al., 2013; Teboul et al., 2019). In Calixto Cave, the colloform-plumose textures and the coexisting solid (S), two-phase (V+L) and single-phase (V) primary inclusions are diagnostic features of hydrothermal processes, possibly associated with boiling solutions (Albinson et al., 2001; Roedder and Bodnar, 1997; Moncada et al., 2017). These features were mainly described in epithermal Au-Ag and precious ore deposits (Sander and Black, 1988; Saunders, 1994; Dong et al., 1995; Camprubí et al., 2007; Moncada et al., 2012; Shimizu, 2014; Palinkaš et al., 2018).

In the Calixto Cave, colloform and plumose textures are typical of qtz-I facies, which represent the first crystallization stage of megaquartz in the paragenetic sequence (Fig. 5, Table 3). Jigsaw mosaic quartz and chalcedony are also associated with dissolution-recrystallization processes of microcrystalline quartz (Sander and Black, 1988; Bobis, 1994; Moncada et al., 2012; Shimizu, 2014). They are mainly associated with a gradually increasing crystal size, as usually observed at the transition between qtz-C and megaquartz and at the rims of the solutional pores in the cherts (Fig. 3b, 3c). The presence of spherulitic/fibrous chalcedony, which is a “rapid” growth texture implying recrystallization of silica, suggests that the fluid was not at high temperature during the formation of this facies (< ca. 150 °C; Marin-Carbonne et al., 2014).

Boiling and resultant quartz textures in epithermal systems (especially colloform quartz) are commonly related to upwelling fluids associated with open channels and accessory ore minerals precipitation (Hedenquist et al., 2000; Simmons et al., 2005; Moncada et al., 2012). Furthermore, silica-rich brecciated textures (like qtz-br facies) are considered a proxy for fluid overpressurization and hydraulic fracturing (Saunders, 1994; Grare et al., 2018).

Solid inclusions compatible with high temperature (likely > 200 °C) parental solutions were found mostly in the early-stage megaquartz (Figs. 4b, 6e). Most of these inclusions consist of sulfates

(anhydrite and barite), sulfides (pyrite and sphalerite), Fe- or Fe-Ti oxides, K-feldspar, muscovite, and apatite (Pisani et al., 2022). Sericitic alteration of K-feldspar associated with sulfide precipitation, as observed in the alteration halos of qtz-br, is typical of high-temperature hydrothermal solutions, close to 200–350 °C (Parry et al., 2002). Furthermore, penecontemporaneous precipitation of sulfides and sulfates may occur at a temperature range of 100 to 500 °C and in alkaline or neutral (pH 7–10) solutions (Zhang, 1986; Rye, 2005). Alkaline (pH > 8–9) conditions and high temperatures are also invoked to explain significant silica dissolution, as evidenced by the widespread karst features in the cherts (Siever, 1962; Mitsiuk, 1974; Dove, 1995; Dove and Nix, 1997; Andreychouk et al., 2009; Cui et al., 2017; Pisani et al., 2022).

The late stage euhedral megaquartz (qtz-II) is characterized by massive or zonal textures (Figs. 5c, 5d), typical of cooling aqueous solutions (Sander and Black, 1988; Moncada et al., 2012, 2017). During the low temperature measurements, evidence of first melting below –40 °C and last melting below the eutectic point of NaCl (–21.2 °C) suggest the presence of antarcticite ($\text{CaCl}_2 \cdot 6\text{H}_2\text{O}$) in the frozen inclusions (Oakes et al., 1990; Goldstein and Reynolds, 1994). Considering the observed phase changes and Raman results at cryogenic temperatures (see section 4.4 and Supplementary Materials), we selected the H_2O -NaCl- CaCl_2 composition as the most likely approximation to assess the salinity for the studied inclusions. Estimated salinity values (Fig. 7b) were calculated from the measured intermediate melting temperature (T_{int}) and final melting temperature (T_{m}) using the Excel spreadsheet provided by Steele-MacInnis et al. (2011). The salinity values are clustered in a narrow range of 17–25 wt.% with only a few individual inclusions showing values < 20 wt.%.

Minimum formation temperature estimates were obtained from primary FIAs homogenization temperatures. Since no independent data on the burial-thermal history are available for the Salitre Fm, we cannot apply a pressure correction (Goldstein and Reynolds, 1994) to the homogenization temperatures. Qtz-II shows primary FIAs with T_{h} of 165–210 °C and high salinity (17–25 wt.%, Fig. 7b). No significant relations have been identified between salinity and T_{h} (Fig. 7c).

The high salinity and the NaCl– CaCl_2 composition of the primary two-phase FIAs suggest extensive fluid-rock interactions, with an enrichment in CaCl_2 likely derived from the interaction with the carbonate-rich strata (Goldstein and Reynolds, 1994; You et al., 2018). Furthermore, the presence of solid inclusions of sulfates, hematite-ilmenite, pyrite, sphalerite, and K-rich silicate (K-feldspar and muscovite), entrapped in the cloudy cores of qtz-I (Figs. 5, 6e), suggest that the estimated H_2O +NaCl+ CaCl_2 composition is likely representative of the latest stages of crystallization,

with the earlier being characterized by an enrichment in other cations (e.g., Fe, Ba, K, Ti), H₂S, and/or SO₄²⁻.

Table 3. Summary of the silica facies at Calixto Cave with associated T_h and salinity values obtained from primary FIAs.

Silica facies	Texture	Primary inclusions T_h	Primary inclusions salinity (wt.%)	Description
qtz-mc	Microcrystalline quartz	<i>n.d.</i>	<i>n.d.</i>	Dolomite replacement; chert nodules and irregular bands; highly porous
qtz-C	Chalcedony or jigsaw mosaic quartz	<i>n.d.</i>	<i>n.d.</i>	Silica recrystallization texture; lining fractures and solutional vugs; gradual transition into qtz-I
qtz-br	Quartz-rich hydraulic breccias	160–185 °C	19–25	Quartz + K-feldspar + sericitic alteration involving overpressurization and hydraulic fracturing
qtz-I	Plumose-colloform megaquartz	<i>n.d.</i>	<i>n.d.</i>	Early stage of megaquartz precipitation, entrapping high temperature solid inclusions
qtz-II	Massive or zonal megaquartz	165–210 °C	17–25	Late stage of megaquartz precipitation

Note: n.d. = not determined.

5.2 Stable isotope modelling and the origin of silicification

Stable isotopes modelling (Stefánsson et al., 2017; Kleine et al., 2018; and references therein) is a common tool used to assess the origin of fluids, chemical reactions, and associated isotope fractionations for various processes occurring in the Earth's crust, including fluid-rock interaction, fluid phase separation (boiling) and cooling.

Silicon isotopes ($\delta^{30}\text{Si}$) are excellent proxies to trace hydrothermal activity and reconstruct paleoenvironments. Generally, the variation range of silicon isotopes during fractionation is very small. For example, the variation of $\delta^{30}\text{Si}$ in ancient sedimentary cherts goes from –5‰ to 5‰, while quartz cements range between –5‰ and 1‰ (Kleine et al., 2018), with negative $\delta^{30}\text{Si}$ values typical of hydrothermal silica precipitation (Robert and Chaussidon, 2006; Abraham et al., 2011).

In this paper, a Rayleigh-type model (see section 3.4, Supplementary Materials and Tab. S3 for further details on the adopted calculations) was applied to simulate equilibrium and kinetic effects on silicon and oxygen isotope variations measured in cherts and quartz deposits in the course of: 1) quartz precipitation from boiling and cooling of hydrothermal fluids; 2) direct quartz precipitation from marine-derived pore water during burial diagenesis; and 3) quartz precipitation from mixing of hydrothermal fluids and seawater.

As shown in Fig. 10, most of the values from Calixto Cave quartz deposits are characterized by relatively negative $\delta^{30}\text{Si}$ values (-2 to 1‰) and relatively positive $\delta^{18}\text{O}$ values (23 to 29‰). The range of measured isotopes for most of the samples is consistent with silica precipitation upon boiling and cooling of Si-rich hydrothermal fluids at temperatures between 110 and 200 °C . The isotopic signature of the hypothetical hydrothermal fluid ($\delta^{30}\text{Si}=6.44\text{‰}$, $\delta^{18}\text{O}=-0.21\text{‰}$) was derived from the Chapada Diamantina basement rocks (in isotopic equilibrium with the fluid at ca. 300 °C). The temperatures assessed for the scenario of boiling/cooling hydrothermal fluids ($T = 140\text{-}200\text{ °C}$) for late-stage megaquartz (qtz-II) are also consistent with the T_h measured for this quartz facies ($T_h = 165\text{-}210\text{ °C}$) (Table 3).

On the contrary, the “pristine” (non-corroded) chert cluster shows positive $\delta^{30}\text{Si}$ ($> 0.1\text{‰}$, mean of 1‰) and $\delta^{18}\text{O}$ values ranging from 22 to 25‰ ; literature data (van den Boorn et al., 2010; Abraham et al., 2011; Chakrabarti et al., 2012; Teboul et al., 2019) consider these values as a possible indicator of direct precipitation from marine-derived pore water during diagenesis. High values of $\delta^{18}\text{O}$ in silica ($> 20\text{-}25\text{‰}$) are usually interpreted in the context of diagenetic fluids (Marin-Carbonne et al., 2014; Teboul et al., 2019), whereas depleted $\delta^{18}\text{O}$ is considered to reflect either a mantle or a meteoric source (Hemond et al., 1993; Kleine et al., 2018). Hydrothermal derived quartz and silica usually show more dispersed $\delta^{18}\text{O}$ values, in the range of $13\text{-}36\text{‰}$ (Clayton et al., 1972; Liu et al., 2022).

The values from uncorroded cherts of the unaltered host rock, clustering in a restricted area (Fig. 10), are inconsistent with the modelled cooling/boiling systematics of hydrothermal fluids. A slightly higher shift in the $\delta^{30}\text{Si}$ (around $+1\text{‰}$) means that this cluster falls outside the predicted domain, suggesting a different parental fluid composition.

Furthermore, a clear trend towards more-depleted $\delta^{30}\text{Si}$ values is observed between the pristine chert and the corroded cherts, showing solutional (vuggy) porosity at the micro-scale. Values of corroded and highly corroded cherts represent samples collected in the middle storey (Fig.

2b), where karstification was stronger and associated with the main conduits of the cave (Pisani et al., 2022).

Fluid-rock interaction resulting in modifications of the pristine isotope ratios of cave walls is a common phenomenon in hypogene speleogenesis (Plan et al., 2012; Spötl et al., 2021; Temovski et al., 2022). The most commonly observed pattern of isotopic alteration in carbonate rocks is the lowering of the bedrock $\delta^{18}\text{O}$ values near the cave wall because of the interaction with low- $\delta^{18}\text{O}$ high temperature meteoric waters, as well as the lowering of bedrock $\delta^{13}\text{C}$ values due to interaction with dissolved inorganic carbon with lower $\delta^{13}\text{C}$ values (Dublyansky, 1995; Temovski et al., 2022). Interaction of low- $\delta^{30}\text{Si}$ and high-temperature thermal solutions with silica material would result in changes in the Si isotopic ratio, usually towards lower $\delta^{30}\text{Si}$ values (Chackrabarti et al., 2012). Many authors, however, suggested that, despite the highly uncertain effect of silica dissolution-recrystallization reactions on Si and O isotopic fractionation, early diagenetic cherts are less susceptible to pervasive post-depositional changes (Knauth, 1979; Heck et al., 2011, Chackrabarti et al., 2012).

In contrast to this assumption, the corroded chert samples in Calixto Cave show evidence of intense post-depositional isotopic alteration ($\delta^{30}\text{Si}$ depletion by up to 3–4‰; $\delta^{18}\text{O}$ increase by up to 6–7‰) that we interpret as the consequence of qtz-mc interacting with deep-seated hydrothermal solutions at high temperature and alkaline conditions, as supported also by textural and petrographic observations (see section 5.1).

To discuss a possible origin for the early-diagenetic cherts, simulation of isotope systematics for silica precipitated from pore (sea)water during diagenesis has been modelled adopting Rayleigh-type fractionation curves (see Supplementary Materials). Trends corresponding to incremental steps of 30 °C in burial temperatures were plotted in dashed red color in Fig. 10, ascribing a region of extremely positive $\delta^{30}\text{Si}$ and $\delta^{18}\text{O}$ values. Since no data are available for the burial-thermal history of the Salitre Fm, these burial temperatures were set arbitrarily to evaluate the consistency of the measured data with the model isotope systematics. Most of the cherts and chalcedony/qtz-I plot in the simulated isotopic range that would imply a burial diagenesis reaching temperatures of 120–150 °C (Fig. 10). In the case of a hypothetical maximum burial temperature of around 150 °C, a cumulative overburden of 4–6 km would be required above the Salitre Fm, assuming an average geothermal gradient of 25–35 °C/km (Kenneth et al., 2012). Nevertheless, such high temperatures would reflect an unrealistic burial depth, exceeding the one estimated for the entire region (Klimchouk et al., 2016, Jaspen et al., 2012).

A study by Japsen et al. (2012) based on apatite fission track data showed that prior to the Campanian the Chapada Diamantina Group (west of the study area) was buried to a depth of no more than 2–3 km. This cover was completely removed during episodic uplift between ca. 80 and 15 Ma (Japsen et al., 2012). However, it is unknown if the Una-Utinga basin was ever buried to the same (or different) depth after the deposition of the Calixto Cave sequence. Hypothesizing a thickness of around 500-1000 m for the Salitre Fm (Misi and Veizer, 1998; Klimchouk et al., 2016), a maximum burial between 2 and 2.5 km could be expected and related to peak temperatures of no more than 60-90 °C under typical geothermal gradients (Kenneth et al., 2012). These values are not supported by the measured isotopes in the cherts and present a discrepancy in temperatures of about 60 °C. Another possibility to fit the isotopic values and predicted temperatures for chert formation with low burial thickness (up to ca. 2.5 km) requires an anomalously high geothermal gradient of 50–60 °C/km.

Since both scenarios seem geologically unlikely, we interpret the early diagenetic chert as the product of precipitation from Precambrian seawater mixed with hydrothermal solutions coming from the basement at relatively low temperature (ca. 50–100 °C; Fig. 10). This process could explain the slightly higher $\delta^{30}\text{Si}$ values that characterize the cherts, shifted towards the $\delta^{30}\text{Si}$ of Precambrian seawater, as predicted by the isotope values modelled for the mixing process (green region in Fig. 10). Most of the values of uncorroded cherts plot close to the lower border of the green shadowed area in the model of Fig. 10, which represent the predicted isotopes for silica precipitation from Precambrian oceanic seawater mixed with low temperature hydrothermal fluids ($T = 50\text{ °C}$). The upper border of the green area represent the predicted isotope systematics of silica precipitated from the same process, but with a hydrothermal fluid temperature reaching 100 °C. This hypothesis is also consistent with the early-diagenetic petrographic characteristics of the cherts (Pisani et al., 2022).



Accepted Article

Accepted Article

Accepted Article

Accepted Article

beyond the scope of this work; however, the subhedral shapes of the dolomite crystals suggest low temperatures and shallow burial conditions (Sibley and Gregg, 1987).

Chert (qtz-mc) in the dolostone layers is interpreted to have formed during a diffuse silicification episode at shallow depth and relatively low temperature (ca. 50–100 °C), by precipitation from ancient seawater mixed with thermal water, sourced from the underlying quartzites of the Chapada Diamantina Group. This process was followed by progressive burial and chemical compaction to form bedding-parallel stylolites.

The process of hydrothermal silicification of carbonates plays an important role in modifying the original petrophysical properties of the rock. Although this effect on porosity is still debated, recent studies on Brazilian pre-salt hydrocarbon reservoirs (Fernández-Ibáñez et al., 2022b) revealed an increase in porosity up to around 10% thanks to hypogene dissolution of mineral grains and the brittle behavior of silica. The localization of fractures in the stiff chert nodules has been observed also in Calixto Cave (Pisani et al., 2022) and contributed to significantly increase porosity and permeability.

Around ca. 600 Ma, the basin was involved in the Brasiliano orogeny, and the depositional environment changed from an intracratonic gulf-like basin to a foreland basin (Santana et al., 2021). Continued burial and tectonic deformation produced a large set of faults and fractures during a prolonged period and the reactivation of basement-rooted structures (D'Angelo et al., 2019). Crustal thickening, continental collision and uplift were marked by an intense magmatic activity, represented by numerous plutons and batholiths that intruded the basement in the orogenic belts surrounding the craton (Ferreira et al., 1998; Sial and Ferreira, 2016). In the Borborema Province (north of the study area), the ages of the plutons fall into two intervals of 640–610 and 590–530 Ma (Guimarães et al., 2004; Neves et al., 2015; Ferreira et al., 2021; Neves et al., 2022). The latest orogenic events in the Cambrian (540–510 Ma) were characterized by hydrothermalism and large-scale fluid migration in the craton (Almeida et al., 2000; Trindade, 2004). Deep-rooted deformation zones represented permeability pathways for the localized upwelling of thermal solutions from the underlying basement rocks (Klimchouk et al., 2016; Bertotti et al., 2020; Pisani et al., 2022).

Evidence of high temperature and alkaline parental solutions explain the widespread dissolution of silica observed in Calixto Cave middle storey, with the development of high solutional porosity and permeability. Bulk permeability in the silicified and karstified layers at Calixto Cave reached 10^3 mD, as reported by Pisani et al. (2022), with rock plugs permeability that can reach up to 200–250 mD (2 to 3 orders of magnitude higher than surrounding carbonates) and porosity up to

16%. The formation of pervasive cavernous porosity-permeability in silica is common in many hydrocarbon reservoirs affected by hydrothermal silicification (Packard et al., 2001; De Luca et al., 2017; Poros et al., 2017; Teboul et al., 2019; Lima et al., 2020; Wei et al., 2021). These reservoirs show incredibly complex porosity-permeability heterogeneities, fault- and fracture-controlled conduit systems, secondary mineralization and reactive fronts associated with vuggy pore space.

Our observations support the previous work of Pisani et al. (2022), who hypothesized that a deep-seated hydrothermal alteration in the cherts caused an increase in porosity and permeability at the micro-scale, which paved the way for the later speleogenetic processes. The combination of high fracture intensity that characterizes the silicified dolostones (Pisani et al., 2022) and early dissolution of silica was crucial for the definition of preferential flow pathways and favorable conditions for hypogene speleogenesis, which ultimately lead to the development of macro-scale conduit-type porosity.

Hydrothermal fluids rising from the underlying Chapada Diamantina Group along faults or fracture zones were the main drivers for hypogene speleogenetic processes in deep-seated confined settings; they determined the formation of extensive networks of conduits in the Salitre Fm, mostly of stratiform and multi-storey type and commonly associated with silica-rich mineralizations (Klimchouk et al., 2016; Cazarin et al., 2019; Balsamo et al., 2020; Bertotti et al., 2020; Pontes et al., 2021; Pisani et al., 2022). In this context, the dissolution of carbonate and silicified layers to form the main conduit networks required specific (and almost opposite) conditions, with the carbonate dissolution promoted by acidic and low temperature conditions, and the silica dissolution promoted by alkaline and/or high temperature conditions (Andreychouk et al., 2009; Cui et al., 2017; Klimchouk, 2019). High temperature aqueous solutions enlarged and connected the vuggy pores in chert nodules, producing micro-scale solutional cavernous voids. Water cooling and/or gradual decrease in pH caused the switch from silica-dominant dissolution to carbonate-dominant dissolution and quartz precipitation.

Euhedral megaquartz (qtz-II) filling fractures and vuggy pores marks the final crystallization stages of the hydrothermal fluids at a minimum temperature range (from homogenization temperatures) of 165–210 °C (Fig. 7a). The decrease in pH towards more acidic conditions is supported not only by the dissolution of the carbonates in the sequence (Pisani et al., 2022), but also by the occurrence of HCO_3^- Raman peaks found in some primary fluid inclusions.

Karstification in hypogene setting to produce the main macro-scale void-conduit systems must have been the result of prolonged dissolution in confined settings, with formation of a three-

dimensional pattern of conduits controlled by the main lateral and vertical heterogeneity in distribution of flow-conducting fractures and, in turn, high- versus low-permeability zones (Klimchouk et al., 2016; Pisani et al., 2022).

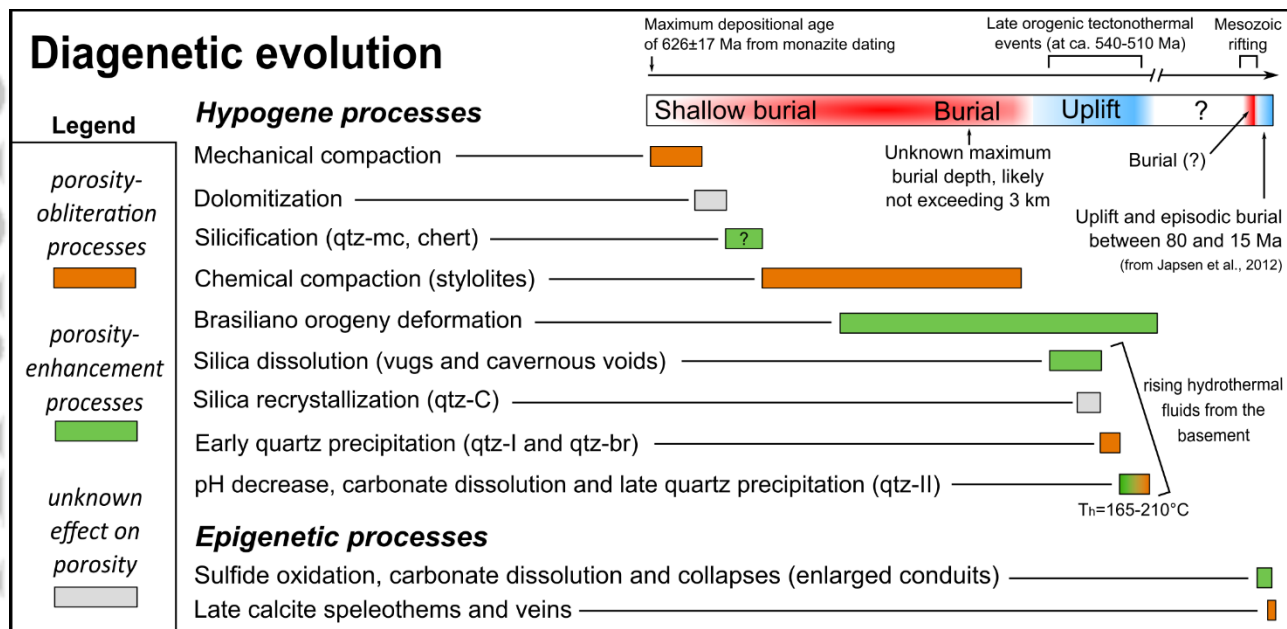


Figure 11. Conceptual scheme of the main diagenetic processes affecting the Calixto Cave sedimentary sequence in relation with the key geodynamic events that occurred in the São Francisco Craton. The main phases of silica dissolution-precipitation are here interpreted as the result of hydrothermal fluid circulation during the Cambrian tectono-thermal events (ca. 540–510 Ma).

5.4 Possible timing of hydrothermal dissolution-precipitation in the Salitre Formation

To constrain the possible age of the hydrothermal dissolution-precipitation phases, monazite grains associated with silicification were dated. The obtained ages (Fig. 9, Table 2) point toward a detrital origin, with ages ranging from Paleoproterozoic (groups 2 and 3) to Neoproterozoic (group 1) source rocks. The maximum depositional age of the Salitre Fm was constrained by the age of the youngest zircon grain at 669 ± 14 Ma by Santana et al. (2021). Our youngest monazite grain (626 ± 17 Ma) further constrains the maximum depositional age of the Calixto Cave sequence to the Ediacaran. In addition, eleven analyses in the same sample are characterized by low Th, U and Pb contents (see section 4.6). This group of monazites, from which no reliable ages could be calculated, might represent detrital grains which have been hydrothermally altered during fluid circulation at the basin scale (Poitrasson et al., 2000) or new (authigenic) hydrothermal crystals. A widespread resetting of the U-Pb isotopic system triggered by hydrothermal fluid circulation was documented

by Trindade et al. (2004) in the Salitre Fm carbonates and dated to the Cambrian (around ca. 520 Ma). The same tectono-thermal event could be related to the hypogene speleogenetic phase affecting the basin, as also suggested by Klimchouk et al. (2016) for the northern sector of the Irecê basin (ca. 330 km north of the study area). There, a giant cave system with similar characteristics to the Calixto Cave has been described (Klimchouk et al., 2016; Cazarin et al., 2019; Balsamo et al., 2020). However, we cannot attribute any definite geochronological constraint to the hydrothermal events affecting the Calixto Cave sequence.

The Cambrian tectono-thermal events recognized in the whole São Francisco and Congo Cratons (Almeida et al., 2000; Trindade et al., 2004; Misi et al., 2005) were regarded by several authors as the source of the Pb-Zn sulfide mineralization in the Salitre Fm (Moraes Filho and Leal, 1990; Kyle and Misi, 1997; Gomes et al., 2000; Silva et al., 2006; Teixeira et al., 2010), and as a possible driver of hypogene (hydrothermal) karst development (Klimchouk et al., 2016; Bertotti et al., 2020). The study of primary fluid inclusions in sphalerites of the Nova Redenção Pb-Zn sulfide deposit (about 20 km to the east of Andaraí city, Fig. 1c) revealed the presence of saline (ca. 24–25 wt.%) aqueous solutions formed mainly by H₂O-NaCl, possibly with dissolved salts of Ca, K or Mg, and minimum trapping temperatures of 140–190 °C (Gomes et al., 2000). This economic ore deposit is in the same basin (Una-Utinga) and is associated with dolostones characterized by silicification and quartz-ferruginous breccias. Primary fluid inclusions in sphalerites from Fe-Zn-Pb ore deposits in the nearby Irecê basin (Kyle and Misi, 1997) point to minimum formation temperatures ranging from 140 to 200 °C. All these ore deposits with gangue quartz mineralization were interpreted as the consequence of hydrothermal fluid circulation in the Salitre Fm during the late phases of the Brasiliano orogeny in the Cambrian. Such observations, reported from different sectors of the craton, are compatible with the petrographic and microthermometric data obtained from the Calixto Cave quartz deposits.

Despite a lack of geochronological constraints, which require additional research, we hypothesize that hypogene silica dissolution (and reprecipitation) likely occurred during the late-orogenic Cambrian tectono-thermal events (Fig. 11). The presence of undulose extinction and deformation lamellae in megaquartz (Figs. 4e, 4f) is also consistent with this interpretation, suggesting that megaquartz precipitation occurred before the Ordovician tectonic stabilization of the cratonic block (Almeida et al., 2000). Another possibility proposed by Klimchouk et al. (2016) is that rifting associated with the Pangea break-up (Triassic–Cretaceous) and its related fluid migration events could be a possible driver for the main phase of hypogene speleogenesis in the Salitre Fm.

If either of these interpretations are correct, the development of solutional (karst) porosity in the silicified rocks of Calixto Cave would be among the oldest studied on Earth (Klimchouk et al., 2016; Auler et al., 2017).

Conclusions

Our petrographic, microthermometric, and stable isotope data suggest that the quartz deposits in the silicified layers of Calixto Cave resulted from interactions with high-temperature hydrothermal solutions. Associated processes involved chert dissolution, chalcedony/quartz reprecipitation lining fractures, and vuggy pores in the sequence. Hydrothermal alteration of the cherts caused a $\delta^{30}\text{Si}$ decrease by up to 3–4‰ in the silicified cherty layers. The isotopic composition of the early diagenetic cherts is explained by precipitation from Neoproterozoic seawater mixed with thermal fluids derived from the quartzites of the Chapada Diamantina basement at an estimated temperature range of 50–100 °C. Chalcedony and megaquartz formed by precipitation from high-temperature hydrothermal fluids show an isotopic signature compatible with boiling/cooling solutions derived from the basement quartzites in the range of 110–200 °C. Further constraints were obtained from microthermometric measurements, which indicate that late-stage megaquartz precipitation happened at a minimum temperature range of 165–210 °C. The dissolved salts in primary FIAs were identified as NaCl-CaCl₂ by low-temperature microthermometric measurements supported by cryogenic Raman spectroscopy. The salinity of the mineral-forming fluids was estimated at 17–25 wt.%. Similar values were also obtained for the quartz-rich hydraulic breccias in the sedimentary units sealing the main conduit system.

The documented dissolution and reprecipitation of silica in Calixto Cave demonstrate the role of hypogene (hydrothermal) processes that drastically modified the petrophysical properties of host rocks considered to have very low solubility at typical near-surface conditions (e.g., chert, quartzite, silicified carbonate). Hydrothermal silicification followed by circulation of high-temperature aqueous fluids in fractured sub-surface systems may promote the formation of high-permeability zones (subsequently filled by chalcedony and mega-quartz). Such peculiar and underestimated processes may have important implications for the development of high porous chert/silicified reservoirs and, potentially, favorable conditions for hypogene speleogenetic processes (e.g., macroscale void-conduit formation).

Despite the high variability of silica sources in sedimentary basins, integrating geochemical, petrographic, and field observations in caves representing analogues of deep-seated conduits, is a

first-order tool to expand our knowledge on hypogene speleogenetic and minerogenetic processes. The research conducted in Calixto Cave may help to clarify the origin of silica dissolution-precipitation processes in other carbonate reservoirs where silicification and karst development are closely associated.

Declaration of Competing Interest

The authors declare that they have no known competing financial interests or personal relationships that could have appeared to influence the work reported in this paper.

Acknowledgments

This research was carried out in association with the ongoing R&D project registered as ANP 20502-1, "*Processos e Propriedades em Reservatórios Carbonáticos Fraturados e Carstificados – POROCARSTE 3D*" (UFRN/UNB/UFRJ/UFC/Shell Brasil/ANP) – Porokarst – Processes and Properties in Fractured and Karstified Carbonate Reservoirs, sponsored by Shell Brasil under the ANP R&D levy as "*Compromisso de Investimento com Pesquisa e Desenvolvimento*". Cave map data were kindly provided by *Grupo Pierre Marin de Espeleologia* (GPME). Cave sampling was performed through SISBIO permit 63178/1. We sincerely thank the Iramaia municipality (State of Bahia) and the Brazilian Federal Environmental Agency (*Instituto Chico Mendes*) for providing access to the cave and the special permission for collecting rock samples.

We thank Bastian Joachim-Mrosko for providing the access to the Raman Spectroscopy Laboratory at the University of Innsbruck and for his valuable help. We also thank Jürgen Konzett for the early discussions on monazite dating and Augusto Auler for the help during fieldwork.

Authorship statement

Luca Pisani: Conceptualization, Methodology, Validation, Investigation (petrography, microthermometry, Raman, Si-O isotopes), Data Curation, Visualization, Supervision, Writing – Original Draft, Writing – Review & Editing; Gabriella Koltai: Methodology, Validation, Investigation (microthermometry), Supervision, Writing – Review & Editing; Yuri Dublyansky: Methodology, Validation, Investigation (microthermometry), Supervision, Writing – Review & Editing; Barbara I. Kleine: Methodology, Investigation (Si-O isotopes), Writing – Review & Editing; Martin J. Whitehouse: Methodology, Investigation (Si-O isotopes); Etienne Skrzypek: Methodology,

Investigation (U-Th-Pb dating), Writing – Review & Editing; Cristina Carbone: Methodology, Investigation (SEM-EDS); Christoph Spötl: Methodology, Validation, Supervision, Writing – Review & Editing; Marco Antonellini: Validation, Supervision, Writing – Review & Editing; Francisco Hilario R. Bezerra: Validation, Supervision, Project Administration, Writing – Review & Editing; Jo De Waele: Conceptualization, Validation, Supervision, Writing – Review & Editing.

Data availability

The data that supports the findings of this study are available in the supplementary material of this article

References

- Abraham, K., Hofmann, A., Foley, S.F., Cardinal, D., Harris, C., Barth, M.G., & Andre, L. (2011). Coupled silicon–oxygen isotope fractionation traces Archaean silicification. *Earth and Planetary Science Letters*, **301**, 222–230. <https://doi.org/10.1016/J.EPSL.2010.11.002>
- Albinson, T., Norman, D.I., Cole, D., & Chomiak, B. (2001). Controls on formation of low-sulfidation epithermal deposits in Mexico; constraints from fluid inclusion and stable isotope data. *Special Publication of the Society of Economic Geologists (U.S.)*, **8**, 1–32.
- Almeida, F.F.M., Brito Neves, B.B., & Dal Rê Carneiro, C. (2000). The origin and evolution of the South American Platform. *Earth-Science Reviews*, **50**, 77–111. [https://doi.org/10.1016/S0012-8252\(99\)00072-0](https://doi.org/10.1016/S0012-8252(99)00072-0).
- Álvaro, J. (2013). Late Ediacaran syn-rift/post-rift transition and related fault-driven hydrothermal systems in the Anti-Atlas Mountains, Morocco. *Basin Research*, **25**, 348–360. <https://doi.org/10.1111/BRE.12003>
- Andreychouk, V., Dublyansky, Y.V., Ezhov, Y., & Lisenin, G. (2009). *Karst in the Earth's Crust: Its Distribution and Principal Types*. University of Silesia — Ukrainian Institute of Speleology and Karstology, Sosnovec–Simferopol, 72 pp.
- Audra, P., Laurent, J.Y., Cailhol, N., Bigot, J.Y., Laurent, D., Vanara, N., Cailhol, D., & Cazenave, G. (2022). Hydrodynamic model for independent cold and thermo-mineral twin springs in a stratified continental karst aquifer, Camou, Arbailles Massif, Pyrénées, France. *International Journal of Speleology*, **51**, 81–91. <https://doi.org/10.5038/1827-806X.51.2.2413>
- Auler, A.S. (2017). Hypogene caves and karst of South America. In: In: Klimchouk, A., Palmer, A.N., De Waele, J., Auler, A.S., Audra, P. (Eds.), *Hypogene Karst Regions and Caves of the World, Cave and Karst Systems of the World*, vol. 2017 Springer International Publishing, Cham. <https://doi.org/10.1007/978-3-319-53348-3>.
- Bakker, R.J. (2004). Raman spectra of fluid and crystal mixtures in the systems H₂O, H₂O–NaCl and H₂O–MgCl₂ at low temperatures: Applications to fluid-inclusion research. *Canadian Mineralogist*, **42**, 1283–1314. <https://doi.org/10.2113/gscanmin.42.5.1283>
- Balsamo, F., Bezerra, F.H.R., Klimchouk, A.B., Cazarin, C.L., Auler, A.S., Nogueira, F.C., & Pontes, C. (2020). Influence of fracture stratigraphy on hypogene cave development and fluid flow anisotropy in layered carbonates, NE Brazil. *Marine and Petroleum Geology*, **114**, 104207. <https://doi.org/10.1016/j.marpetgeo.2019.104207>

- Bence, A.E., & Albee, A.L. (1968). Empirical correction factors for the electron microanalysis of silicates and oxides. *Journal of Geology*, **76**, 382–403.
- Bennett, P.C., Melcer, M.E., Siegel, D.I., & Hassett, J.P. (1988). The dissolution of quartz in dilute aqueous solutions of organic acids at 25°C. *Geochimica et Cosmochimica Acta*, **52**, 1521–1530. [https://doi.org/10.1016/0016-7037\(88\)90222-0](https://doi.org/10.1016/0016-7037(88)90222-0)
- Bento dos Santos, T.M., Tassinari, C.C.G., & Fonseca, P.E. (2015). Diachronic collision, slab break-off and long-term high thermal flux in the Brasiliano–Pan-African orogeny: Implications for the geodynamic evolution of the Mantiqueira Province. *Precambrian Research*, **260**, 1–22. <https://doi.org/10.1016/J.PRECAMRES.2014.12.018>
- Bertotti, G., Audra, P., Auler, A., Bezerra, F.H., de Hoop, S., Pontes, C., Prabhakaran, R., & Lima, R. (2020). The Morro Vermelho hypogenic karst system (Brazil): Stratigraphy, fractures, and flow in a carbonate strike-slip fault zone with implications for carbonate reservoirs. *AAPG Bulletin*, **104**, 2029–2050. <https://doi.org/10.1306/05212019150>
- Bobis, R.E. (1994). A review of the description, classification and origin of quartz textures in low sulphidation epithermal veins. *Journal of the Geological Society of the Philippines*, **49**, 15–39.
- Bodnar, R.J. (2003.) Reequilibration of Fluid Inclusions. In: Samson, I., Anderson, A., and Marshall, D. (Eds.), *Fluid inclusions: Analysis and Interpretation*. Mineralogical Association of Canada, 213–230.
- Brito Neves, B.B., Fuck, R.A., & Martins, M. (2014). The Brasiliano collage in South America: a review. *Brazilian Journal of Geology*, **44**, 493–518.
- Caird, R.A., Pufahl, P.K., Hiatt, E.E., Abram, M.B., Rocha, A.J.D., & Kyser, T.K. (2017). Ediacaran stromatolites and intertidal phosphorite of the Salitre Formation, Brazil: Phosphogenesis during the Neoproterozoic Oxygenation Event. *Sedimentary Geology*, **350**, 55–71. <https://doi.org/10.1016/j.sedgeo.2017.01.005>
- Camprubí, A., & Albinson, T. (2007). Epithermal deposits in México - Update of current knowledge and an empirical reclassification. *Special Paper of the Geological Society of America*, **422**, 377–415. [https://doi.org/10.1130/2007.2422\(14\)](https://doi.org/10.1130/2007.2422(14))
- Cazarin, C.L., Bezerra, F.H.R., Borghi, L., Santos, R.V., Favoreto, J., Brod, J.A., Auler, A.S., & Srivastava, N.K. (2019). The conduit-seal system of hypogene karst in Neoproterozoic carbonates in northeastern Brazil. *Marine and Petroleum Geology*, **101**, 90–107. <https://doi.org/10.1016/j.marpetgeo.2018.11.046>
- Cazarin, C.L., van der Velde, R., Santos, R.V., Reijmer, J.J.G., Bezerra, F.H.R., Bertotti, G., La Bruna, V., Silva, D.C.C., de Castro, D.L., Srivastava, N.K., & Barbosa, P.F. (2021). Hydrothermal activity along a strike-slip fault zone and host units in the São Francisco Craton, Brazil – Implications for fluid flow in sedimentary basins. *Precambrian Research*, **365**, 106365. <https://doi.org/10.1016/J.PRECAMRES.2021.106365>
- Chakrabarti, R., Knoll, A.H., Jacobsen, S.B., & Fischer, W.W. (2012). Si isotope variability in Proterozoic cherts. *Geochimica et Cosmochimica Acta*, **91**, 187–201. <https://doi.org/10.1016/J.GCA.2012.05.025>
- Choquette, P.W., & Pray, L.C. (1970). Geologic Nomenclature and Classification of Porosity in Sedimentary Carbonates. *AAPG Bulletin*, **54**, 207–250.
- Clayton, R.N., O'Neil, J.R., & Mayeda, T.K. (1972). Oxygen isotope exchange between quartz and water. *Journal of Geophysical Research*, **77**, 3057–3067
- Cui, H., Kaufman, A.J., Xiao, S., Zhou, C., & Liu, X.M. (2017). Was the Ediacaran Shuram Excursion a globally synchronized early diagenetic event? Insights from methane-derived authigenic carbonates in the uppermost Doushantuo Formation, South China. *Chemical Geology*, **450**, 59–80. <https://doi.org/10.1016/j.chemgeo.2016.12.010>

- D'Angelo, T., Barbosa, M.S.C., & Danderfer Filho, A. (2019). Basement controls on cover deformation in eastern Chapada Diamantina, northern São Francisco Craton, Brazil: Insights from potential field data. *Tectonophysics*, **772**, 228231. <https://doi.org/10.1016/j.tecto.2019.228231>
- De Luca, P.H.V., Matias, H., Carballo, J., Sineva, D., Pimentel, G.A., Tritlla, J., Esteban, M., Loma, R., Alonso, J.L.A., Jiménez, R.P., Pontet, M., Martinez, P.B., & Vega, V. (2017). Breaking barriers and paradigms in presalt exploration: The Pão de Açúcar discovery (Offshore Brazil). *AAPG Memoir*, **113**, 177–193. <https://doi.org/10.1306/13572007M1133686>.
- Dong, G., Morrison, G., & Jaireth, S. (1995). Quartz textures in epithermal veins, Queensland - classification, origin, and implication. *Economic Geology*, **90**, 1841–1856. <https://doi.org/10.2113/gsecongeo.90.6.1841>
- Dong, S., You, D., Guo, Z., Guo, C., & Chen, D. (2018). Intense silicification of Ordovician carbonates in the Tarim Basin: constraints from fluid inclusion Rb–Sr isotope dating and geochemistry of quartz. *Terra Nova*, **30**, 406–413. <https://doi.org/10.1111/ter.12356>.
- Dove, P.M. (1995). Kinetic and thermodynamic controls on silica reactivity in weathering environments. In: White A. F., Brantley S. L. (Eds.), Reviews in Mineralogy 31, *Chemical Weathering Rates of Silicate Minerals*, Berlin, De Gruyter & Co., 235–291.
- Dove, P.M., & Nix, C.J. (1997). The influence of the alkaline earth cations, magnesium, calcium, and barium on the dissolution kinetics of quartz. *Geochimica et Cosmochimica Acta*, **61**(16), 3329–3340. [https://doi.org/10.1016/S0016-7037\(97\)00217-2](https://doi.org/10.1016/S0016-7037(97)00217-2)
- Dubessy, J., Buschaert, S., Lamb, W., Pironon, J., & Thiéry, R. (2001). Methane-bearing aqueous fluid inclusions: Raman analysis, thermodynamic modelling and application to petroleum basins. *Chemical Geology*, **173**, 193–205. [https://doi.org/10.1016/S0009-2541\(00\)00275-8](https://doi.org/10.1016/S0009-2541(00)00275-8)
- Dublyansky, Y.V. (1990). Zakonomernosti formirovaniya i modelirovaniye gidrotermokarsta (*Particularities of the development and modeling of hydrothermal karst*). Nauka, Novosibirsk, 151 pp.
- Dublyansky, Y.V. (1995). Speleogenetic history of the Hungarian hydrothermal karst. *Environmental Geology*, **25**, 24–35.
- Fernández-Ibáñez, F., Jones, G.D., Mimoun, J.G., Bowen, M.G., Simo, J.A.T., Marcon, V., & Esch, W.L. (2022a). Excess permeability in the Brazil pre-Salt: Non matrix types, concepts, diagnostic indicators, and reservoir implications. *AAPG Bulletin*, **106**, 701–738. <https://doi.org/10.1306/10042120171>
- Fernández-Ibáñez, F., Nolting, A., Breithaupt, C.I., Darby, B., Mimoun, J., & Henares, S. (2022b). The properties of faults in the Brazil pre-salt: A reservoir characterization perspective. *Marine and Petroleum Geology*, **146**, 105955. <https://doi.org/10.1016/J.MARPETGEO.2022.105955>
- Ferreira, V.P., Sial, A.N., & Jardim de Sà, E.F. (1998). Geochemical and isotopic signatures of Proterozoic granites in terranes of the Borborema structural province, northeast Brazil. *Journal of South American Earth Sciences*, **11**(5), 439–455.
- Ferreira, A.C., Dantas, E.L., Fuck, R.A., Nedel, I.M., & Reimold, W.U. (2021). Multiple stages of migmatite generation during the Archean to Proterozoic crustal evolution in the Borborema Province, Northeast Brazil. *Gondwana Research*, **90**, 314–334.
- Girard, J.P., & San Miguel, G. (2017). Evidence of high temperature hydrothermal regimes in the pre-salt series, Kwanza Basin, offshore Angola. In: American Association of Petroleum Geologists Annual Convention and Exhibition (Houston, Texas, USA, Abstracts).
- Goldscheider, N., Mádl-Szőnyi, J., Erőss, A., & Schill, E. (2010). Thermal water resources in carbonate rock aquifers. *Hydrogeology Journal*, **18**, 1303–1318.
- Goldstein, R.H. (2003). Petrographic analysis of fluid inclusions. In: Samson, I., Anderson, A., and Marshall, D. (Eds.), *Fluid inclusions: Analysis and Interpretation*, Mineralogical Association of Canada, 1–45.

- Goldstein, R.H., & Reynolds, T.J. (1994). *Systematics of Fluid Inclusions in Diagenetic Minerals*. Soc. Sed. Geol. Short Course 31, 199 pp.
- Gomes, A.S.R., Coelho, C.E.S., & Misi, A. (2000). Fluid Inclusion Investigation of the Neoproterozoic Lead-Zinc Sulfide Deposit of Nova Redenção, Bahia, Brazil. *Revista Brasileira de Geociências*, **30**, 315–317. <https://doi.org/10.25249/0375-7536.2000302315317>
- Grare, A., Lacombe, O., Mercadier, J., Benedicto, A., Guilcher, M., Trave, A., Ledru, P., & Robbins, J. (2018). Fault zone evolution and development of a structural and hydrological barrier: The quartz breccia in the Kiggavik area (Nunavut, Canada) and its control on uranium mineralization. *Minerals*, **8**, 1–28. <https://doi.org/10.3390/min8080319>
- Guimarães, I.P., Da Silva Filho, A.F., Almeida, C.N., Van Schmus, W.R., Araújo, J.M.M., Melo, S.C., & Melo, E.B. (2004). Brasiliano (Pan-African) granitic magmatism in the Pajeú-Paraíba belt, Northeast Brazil: an isotopic and geochronological approach. *Precambrian Research*, **135**, 23–53. <https://doi.org/10.1016/J.PRECAMRES.2004.07.004>
- Guimarães, J.T., Misi, A., Pedreira, A.J., & Dominguez, J.M.L. (2011). The Bebedouro formation, Una Group, Bahia (Brazil). *Geological Society of London Memoirs*, **36**, 503–508. <https://doi.org/10.1144/M36.47>
- Heck, P.R., Huberty, J.M., Kita, N.T., Ushikubo, T., Kozdon, R., & Valley, J.W. (2011). SIMS analyses of silicon and oxygen isotope ratios for quartz from Archean and Paleoproterozoic banded iron formations. *Geochimica et Cosmochimica Acta*, **75**, 5879–5894.
- Hedenquist, J.W., Arribas, R.A., & Gonzalez-Urien, E. (2000). Exploration for epithermal gold deposits. *Reviews in Economic Geology*, **13**, 245–277.
- Hemond, C., Arndt, N.T., Lichtenstein, U., Hofmann, A.W., Oskarsson, N., & Steinthorsson, S. (1993). The heterogeneous Iceland plume: Nd Sr O isotopes and trace element constraints. *Journal of Geophysical Research: Solid Earth*, **98**, 15833–15850.
- Hesse, R. (1989). Silica diagenesis: origin of inorganic and replacement cherts. *Earth-Science Reviews*, **26**, 253–284. [https://doi.org/10.1016/0012-8252\(89\)90024-X](https://doi.org/10.1016/0012-8252(89)90024-X)
- Japsen, P., Bonow, J.M., Green, P.F., Cobbold, P.R., Chiossi, D., Lilletveit, R., Magnavita, L.P., & Pedreira, A.J. (2012). Episodic burial and exhumation history of NE Brazil after opening of the south Atlantic. *GSA Bulletin*, **124**, 800–816. <http://dx.doi.org/10.1130/B30515.1>
- Kato, T. (2005). New accurate Bence-Albee α -factors for oxides and silicates calculated from the PAP correction procedure. *Geostandards and Geoanalytical Research*, **29**, 83–94.
- Kleine, B.I., Stefánsson, A., Halldórsson, S.A., Whitehouse, M.J., & Jónasson, K. (2018). Silicon and oxygen isotopes unravel quartz formation processes in the Icelandic crust. *Geochemical Perspectives Letters*, **7**, 5–11. <https://doi.org/10.7185/geochemlet.1811>
- Klimchouk A. (2007). *Hypogene speleogenesis: hydrogeological and morphometric perspective*. Carlsbad, National Cave and Karst Research Institute, 106 pp.
- Klimchouk, A. (2019). Speleogenesis, hypogenic. In: White, W.B., Culver, D.C., Pipan, T. (Eds.), *Encyclopedia of Caves*, 3rd edition. Academic Press, New York, 974–988.
- Klimchouk, A., Auler, A.S., Bezerra, F.H.R., Cazarin, C.L., Balsamo, F., & Dublyansky, Y. (2016). Hypogenic origin, geologic controls, and functional organization of a giant cave system in Precambrian carbonates, Brazil. *Geomorphology*, **253**, 385–405. <https://doi.org/10.1016/j.geomorph.2015.11.002>
- Knauth, L.P. (1979). A model for the origin of chert in limestone. *Geology*, **7**(6), 274–277.
- Kornilov, V.F. (1978). The temperature regime of formation of the mercury–antimony mineralization (Southern Kirghizia). In: Ermakov, N.P. (Ed.), *Thermobarogeochemistry of the Earth's Crust*. Nauka, Moscow, 155–161.

- Kyle, J.R., & Misi, A. (1997). Origin of Zn-Pb-Ag sulfide mineralization within upper proterozoic phosphate-rich carbonate strata, Irêce Basin, Bahia, Brazil. *International Geology Review*, **39**, 383–399.
- La Bruna, V., Bezerra, F.H.R., Souza, V.H.P., Maia, R.P., Auler, A.S., Araújo, R.E.B., Cazarin, C.L., Rodrigues, M.A.F., Vieira, L.C., & Sousa, M.O.L. (2021). High-permeability zones in folded and faulted silicified carbonate rocks – Implications for karstified carbonate reservoirs. *Marine and Petroleum Geology*, **128**, 105046. <https://doi.org/10.1016/j.marpetgeo.2021.105046>
- Ledevin, M., Arndt, N., Chauvel, C., Jaillard, E., & Simionovici, A. (2019). The sedimentary origin of black and white banded cherts of the Buck Reef, Barberton, South Africa. *Geosciences*, **9**, 17–24. <https://doi.org/10.3390/geosciences9100424>
- Leven, J.A. (1961). Problems of origin of optical-quality fluorite from deposits of the Zeravshan–Gissar Mountains. *Trans. Samarkand Univ.* 16, 35–51.
- Lima, B.E.M., & De Ros, L.F. (2019). Deposition, diagenetic and hydrothermal processes in the Aptian Pre-Salt lacustrine carbonate reservoirs of the northern Campos Basin, offshore Brazil. *Sedimentary Geology*, **383**, 55–81. <https://doi.org/10.1016/j.sedgeo.2019.01.006>.
- Lima, B.E.M., Tedeschi, L.R., Pestilho, A.L.S., Santos, R.V., Vazquez, J.C., Guzzo, J.V.P., & De Ros, L.F. (2020). Deep-burial hydrothermal alteration of the Pre-Salt carbonate reservoirs from northern Campos Basin, offshore Brazil: evidence from petrography, fluid inclusions, Sr, C and O isotopes. *Marine and Petroleum Geology*, **113**, 104143. <https://doi.org/10.1016/j.marpetgeo.2019.104143>.
- Liu, C., Ma, J., Zhang, L., Wang, C., & Liu, J. (2022). Protracted formation of nodular cherts in marine platform: new insights from the Middle Permian Chihshian carbonate successions, South China. *Carbonates and Evaporites*, **37**, 1–19. <https://doi.org/10.1007/S13146-022-00757-6/FIGURES/10>
- Lovering, T.S., Tweto, O., & Loweing, T.G. (1978). Ore deposits of the Gilman District, Eagle Country, Colorado. *U.S. Geological Survey Professional Paper*, **1017**, 90 pp.
- Magalhães, A.J.C., Raja Gabaglia, G.P., Scherer, C.M.S., Bállico, M.B., Guadagnin, F., Bento Freire, E., Silva Born, L.R., & Catuneanu, O. (2016). Sequence hierarchy in a Mesoproterozoic interior sag basin: from basin fill to reservoir scale, the Tombador Formation, Chapada Diamantina Basin, Brazil. *Basin Research*, **28**, 393–432. <https://doi.org/10.1111/BRE.12117>
- Maliva, R.G., & Siever, R. (1989). Nodular Chert Formation in Carbonate Rocks. *Journal of Geology*, **97**, 421–433.
- Maliva, R.G., Knoll, A.H., & Simonson, B.M. (2005). Secular change in the Precambrian silica cycle: Insights from chert petrology. *GSA Bulletin*, **117**, 835–845. <https://doi.org/10.1130/B25555.1>
- Marchesini, B., Garofalo, P.S., Menegon, L., Mattila, J., & Viola, G. (2019). Fluid-mediated, brittle-ductile deformation at seismogenic depth - Part 1: Fluid record and deformation history of fault veins in a nuclear waste repository (Olkiluoto Island, Finland). *Solid Earth*, **10**, 809–838. <https://doi.org/10.5194/se-10-809-2019>
- Marin, J. (2009). Composition isotopique de l’oxygène et du silicium dans les cherts Précambriens : Implications Paléo-environnementales. PhD thesis. Institut National Polytechnique de Lorraine, 402 pp.
- Marin-Carbonne, J., Faure, F., Chaussidon, M., Jacob, D., & Robert, F. (2013). A petrographic and isotopic criterion of the state of preservation of Precambrian cherts based on the characterization of the quartz veins. *Precambrian Research*, **231**, 290–300.
- Marin-Carbonne, J., Robert, F., & Chaussidon, M. (2014). The silicon and oxygen isotope compositions of Precambrian cherts: A record of oceanic paleo-temperatures? *Precambrian Research*, **247**, 223–234. <https://doi.org/10.1016/j.precamres.2014.03.016>

- Misi, A., & Veizer, J. (1998). Neoproterozoic carbonate sequences of the Una Group, Irêce Basin, Brazil: chemostratigraphy, age and correlations. *Precambrian Research*, **89**, 87–100. [https://doi.org/10.1016/S0301-9268\(97\)00073-9](https://doi.org/10.1016/S0301-9268(97)00073-9).
- Misi, A., Iyer, S.S.S., Coelho, C.E.S., Tassinari, C.C.G., Franca-Rocha, W.J.S., Cunha, I.D.A., Gomes, A.S.R., de Oliveira, T.F., Teixeira, J.B.G., & Filho, V.M.C. (2005). Sediment hosted lead–zinc deposits of the Neoproterozoic Bambuí Group and correlative sequences, São Francisco craton, Brazil: a review and a possible metallogenic evolution model. *Ore Geology Reviews*, **26**, 263–304.
- Misi, A., Kaufman, A.J., Veizer, J., Powis, K., Azmy, K., Boggiani, P.C., Gaucher, C., Teixeira, J.B.G., Sanches, A.L., & Iyer, S.S. (2007). Chemostratigraphic correlation of Neoproterozoic successions in South America. *Chemical Geology*, **237**, 22–45. <http://dx.doi.org/10.1016/j.chemgeo.2006.06.019>.
- Misi, A., Kaufman, A.J., Azmy, K., & Dardenne, M.A. (2011). Neoproterozoic successions of the São Francisco craton, Brazil: The Bambuí, Una, Vazante and Vaza Barris/Miaba groups and their glaciogenic deposits. *Geological Society of London Memoirs*, **36**, 509–522. <https://doi.org/10.1144/M36.48>.
- Misi, A., Batista, J., & Teixeira, G. (2012). Mapa Metalogenético Digital do Estado da Bahia e Principais Províncias Minerais. Série Publicações Especiais 11.
- Mitsiuk, B.N. (1974). Vzaimodeistvie kremnezema s vodoy v hydrotermalnykh usloviakh (*Interaction between silica and water in hydrothermal conditions*). In: Naukova Dumka, Kiev, 86 pp.
- Moncada, D., Mutchler, S., Nieto, A., Reynolds, T.J., Rimstidt, J.D., & Bodnar, R.J. (2012). Mineral textures and fluid inclusion petrography of the epithermal Ag–Au deposits at Guanajuato, Mexico: Application to exploration. *Journal of Geochemical Exploration*, **114**, 20–35. <https://doi.org/10.1016/J.GEXPLO.2011.12.001>
- Moncada, D., Baker, D., & Bodnar, R.J. (2017). Mineralogical, petrographic and fluid inclusion evidence for the link between boiling and epithermal Ag–Au mineralization in the La Luz area, Guanajuato Mining District, México. *Ore Geology Reviews*, **89**, 143–170. <https://doi.org/10.1016/j.oregeorev.2017.05.024>
- Montanari, D., Minissale, A., Doveri, M., Gola, G., Trumphy, E., Santilano, A., & Manzella, A. (2017). Geothermal resources within carbonate reservoirs in western Sicily (Italy): A review. *Earth-Science Reviews*, **169**, 180–201. <https://doi.org/10.1016/J.EARSCIREV.2017.04.016>
- Montel, J. M., Foret, S., Veschambre, M., Nicollet, C., & Provost, A. (1996). Electron microprobe dating of monazite. *Chemical Geology*, **131**(1-4), 37–53.
- Moraes Filho, O., & Leal, R.A. (1990). Lead-zinc-silver search in the municipal district of Nova Redenção (BA). In: *Anais 36º Congresso Brasileiro de Geologia*, 1990, Natal, 1487–1501.
- Neves, S.P., Lages, G.A., Brasilino, R.G., & Miranda, A.W.A. (2015). Paleoproterozoic accretionary and collisional processes and the build-up of the Borborema Province (NE Brazil): Geochronological and geochemical evidence from the Central Domain. *Journal of South American Earth Sciences*, **58**, 165–187. <https://doi.org/10.1016/J.JSAMES.2014.06.009>
- Neves, S.P., Teixeira, C.M.L., Silva, V.L., Bruguier, O. (2022). Protracted (>60 Myrs) thermal evolution of a Neoproterozoic metasedimentary sequence from eastern Borborema Province (NE Brazil): Thermal and rheological implications for orogenic development. *Precambrian Research*, **377**, 106709. <https://doi.org/10.1016/J.PRECAMRES.2022.106709>
- Oakes, C.S., Bodnar, R.J., & Simonson, J.M. (1990). The system NaCl–CaCl₂–H₂O: I. The ice liquidus at 1 atm total pressure. *Geochimica et Cosmochimica Acta*, **54**, 603–610.
- Onac, B.P., & Forti, P. (2011). Minerogenetic mechanisms occurring in the cave environment: An overview. *International Journal of Speleology*, **40**, 79–98. <https://doi.org/10.5038/1827-806X.40.2.1>

- Packard, J.J., Al-Aasm, I., Samson, I. (2001). A Devonian hydrothermal chert reservoir: The 225 bcf Parkland field, British Columbia, Canada. *AAPG Bulletin*, **85**(1), 51–84.
- Palinkaš, S.S., Hofstra, A.H., Percival, T.J., Šoštarkć, S.B., Palinkaš, L., Bermanec, V., Pecskay, Z., & Boev, B. (2018). Comparison of the Allchar Au-As-Sb-Tl Deposit, Republic of Macedonia, with Carlin-Type Gold Deposits. In: John L. Muntean (Ed.), *Diversity in Carlin-Style Gold Deposits*, Reviews in Economic Geology vol. 20, Society of Economic Geologists, Littleton, USA, 353–363.
- Parry, W. T., Jasumback, M., & Wilson, P. N. (2002). Clay Mineralogy of Phyllic and Intermediate Argillic Alteration at Bingham, Utah. *Economic Geology*, **97**(2), 221–239. <https://doi.org/10.2113/GSECONGEO.97.2.221>
- Passchier, C. W., & Trouw, R. A. (2005). *Microtectonics*. Springer Science & Business Media.
- Pisani, L., Antonellini, M., Bezerra, F.H.R., Carbone, C., Auler, A.S., Audra, P., La Bruna, V., Bertotti, G., Balsamo, F., Pontes, C.C.C., & De Waele, J. (2022). Silicification, flow pathways, and deep-seated hypogene dissolution controlled by structural and stratigraphic variability in a carbonate-siliciclastic sequence (Brazil). *Marine and Petroleum Geology*, **139**, 105611. <https://doi.org/10.1016/J.MARPETGEO.2022.105611>
- Plan, L., Tschegg, C., De Waele, J., & Spötl, C. (2012). Corrosion morphology and cave wall alteration in an Alpine sulfuric acid cave (Kraushöhle, Austria). *Geomorphology*, **169–170**, 45–54. <https://doi.org/10.1016/J.GEOMORPH.2012.04.006>
- Poitrasson, F., Chenery, S., & Shepherd, T.J. (2000). Electron microprobe and LA-ICP-MS study of monazite hydrothermal alteration: Implications for U-Th-Pb geochronology and nuclear ceramics. *Geochimica et Cosmochimica Acta*, **64**, 3283–3297. [https://doi.org/10.1016/S0016-7037\(00\)00433-6](https://doi.org/10.1016/S0016-7037(00)00433-6)
- Pollock, S.G. (1987). Chert formation in an Ordovician volcanic arc. *Journal of Sedimentary Petrology*, **57**(1), 75–87.
- Pontes, C.C.C., Bezerra, F.H.R., Bertotti, G., La Bruna, V., Audra, P., De Waele, J., Auler, A.S., Balsamo, F., De Hoop, S., & Pisani, L. (2021). Flow pathways in multiple-direction fold hinges: implications for fractured and karstified carbonate reservoirs. *Journal of Structural Geology*, **146**, 104324. <https://doi.org/10.1016/j.jsg.2021.104324>
- Poros, Z., Jagniecki, E., Luczaj, J., Kenter, J., Gal, B., Correa, T.S., Ferreira, E., McFadden, K.A., Elifritz, A., Heumann, M., Johnston, M., & Matt, V. (2017). Origin of silica in pre-salt carbonates, Kwanza Basin, Angola. In: *American Association of Petroleum Geologists Annual Convention and Exhibition*, Houston, Texas (USA).
- Rimstidt, J.D. (1997). Quartz solubility at low temperatures. *Geochimica et Cosmochimica Acta*, **61**, 2553–2558.
- Robert, F., & Chaussidon, M. (2006). A palaeotemperature curve for the Precambrian oceans based on silicon isotopes in cherts. *Nature*, **443**, 969–972.
- Roedder, E. (1984). *Fluid inclusions*. In: Reviews in Mineralogy 12, ed. Mineralogical Society of America, 646.
- Roedder, E., & Bodnar, R.J. (1997). Fluid inclusion studies of hydrothermal ore deposits. In: Barnes, H.L. (Ed.), *Geochemistry of Hydrothermal Ore Deposits*. Wiley, New York, 657–697.
- Rye, R.O. (2005). A review of the stable-isotope geochemistry of sulfate minerals in selected igneous environments and related hydrothermal systems. *Chemical Geology*, **215**, 5–36. <https://doi.org/10.1016/j.chemgeo.2004.06.034>
- Samson, I.M., & Walker, R.T. (2000). Cryogenic raman spectroscopic studies in the system NaCl-CaCl₂-H₂O and implications for low-temperature phase behavior in aqueous fluid inclusions. *Canadian Mineralogist*, **38**, 35–43. <https://doi.org/10.2113/gscanmin.38.1.35>

- Sander, M. V., & Black, J.E. (1988). Crystallization and recrystallization of growth-zoned vein quartz crystals from epithermal systems; implications for fluid inclusion studies. *Economic Geology*, **83**, 1052–1060.
- Santana, A., Chemale, F., Scherer, C., Guadagnin, F., Pereira, C., & Santos, J.O.S. (2021). Paleogeographic constraints on source area and depositional systems in the Neoproterozoic Irecê Basin, São Francisco Craton. *Journal of South American Earth Sciences*, **109**, 103330. <https://doi.org/10.1016/j.jsames.2021.103330>
- Saunders, J.A. (1994). Silica and gold textures in bonanza ores of the sleeper deposit, Humboldt County, Nevada: Evidence for colloids and implications for epithermal ore-forming processes. *Economic Geology*, **89**, 628–638. <https://doi.org/10.2113/gsecongeo.89.3.628>
- Sauro, F., De Waele, J., Onac, B.P., Galli, E., Dublyansky, Y., Baldoni, E., & Sanna, L. (2014). Hypogenic speleogenesis in quartzite: The case of Corona 'e Sa Craba Cave (SW Sardinia, Italy). *Geomorphology*, **211**, 77–88. <https://doi.org/10.1016/j.geomorph.2013.12.031>
- Seitz, S., Baumgartner, L.P., Bouvier, A.S., Putlitz, B., & Vennemann, T. (2017). Quartz Reference Materials for Oxygen Isotope Analysis by SIMS. *Geostandards and Geoanalytical Research*, **41**, 69–75.
- Shanmugan, G., & Higgins, J.B. (1988). Porosity enhancement from chert dissolution beneath Neocomian unconformity: Ivishak Formation, North Slope, Alaska. *AAPG Bulletin*, **72**(5), 523–535.
- Shimizu, T. (2014). Reinterpretation of quartz textures in terms of hydrothermal fluid evolution at the Koryu Au-Ag deposit, Japan. *Economic Geology*, **109**, 2051–2065.
- Sial, A.N., & Ferreira, V.P. (2016). Magma associations in Ediacaran granitoids of the Cachoeirinha–Salgueiro and Alto Pajeú terranes, northeastern Brazil: Forty years of studies. *Journal of South American Earth Sciences*, **68**, 113–133. <https://doi.org/10.1016/J.JSAMES.2015.10.005>
- Sial, A.N., Gaucher, C., Misi, A., Boggiani, P.C., De Alvarenga, C.J.S., Ferreira, V.P., Pimentel, M.M., Pedreira, J.A., Warren, L.V., Fernández-Ramírez, R., Geraldés, M., Pereira, N.S., Chiglino, L., & Dos Santos Cezario, W. (2016). Correlations of some Neoproterozoic carbonate-dominated successions in South America based on high-resolution chemostratigraphy, *Brazilian Journal of Geology*, **46**(3), 439–388. <https://doi.org/10.1590/2317-4889201620160079>
- Sibley, D.F., & Gregg, J.M. (1987). Classification of dolomite rock textures. *Journal of Sedimentary Research*, **57**, 967–975. <https://doi.org/10.1306/212F8CBA-2B24-11D7-8648000102C1865D>
- Siever, R. (1962). Silica solubility, 0°C - 200°C, and the diagenesis of siliceous sediments. *Journal of Geology*, **70**, 127–150.
- Siever, R., & Woodford, N. (1973). Sorption of silica by clay minerals. *Geochimica et Cosmochimica Acta*, **37**, 1851–1880.
- Silva, M.G., Neves, J.P., Klein, E., Bento, R.V., & Dias, V.M. (2006). Principais processos envolvidos na gênese das mineralizações de Sn, Au, Ba, quartzo rutilado e diamante, na região do Espinhaço-Chapada Diamantina, Bahia. In: *Anais 43º Congresso Brasileiro de Geologia*, 2006, Aracaju, 381.
- Simmons, S.F., White, N.C., & John, D.A. (2005). Geological characteristics of epithermal precious and base metal deposits. In: *Economic Geology: One Hundredth Anniversary Volume 1905–2005*, 485–522.
- Souza, V.H.P., Bezerra, F.H.R., Vieira, L.C., Cazarin, C.L., & Brod, J.A. (2021). Hydrothermal silicification confined to stratigraphic layers: Implications for carbonate reservoirs. *Marine and Petroleum Geology*, **124**, 104818. <https://doi.org/10.1016/j.marpetgeo.2020.104818>
- Spötl, C., Dublyansky, Y., Koltai, G., & Cheng, H. (2021). Hypogene speleogenesis and paragenesis in the Dolomites. *Geomorphology*, **382**, 107667. <https://doi.org/10.1016/J.GEOMORPH.2021.107667>

- Steele-MacInnis, M., Bodnar, R.J., & Naden, J. (2011). Numerical model to determine the composition of H₂O–NaCl–CaCl₂ fluid inclusions based on microthermometric and microanalytical data. *Geochimica et Cosmochimica Acta*, **75**, 21–40.
- Stefánsson, A., Hilton, D.R., Sveinbjörnsdóttir, Á.E., Torssander, P., Heinemeier, J., Barnes, J.D., Ono, S., Halldórsson, S.A., Fiebig, J., & Arnórsson, S. (2017). Isotope systematics of Icelandic thermal fluids. *Journal of Volcanology and Geothermal Research*, **337**, 146–164. <https://doi.org/10.1016/J.JVOLGEORES.2017.02.006>
- Strugale, M., & Cartwright, J. (2022). Tectono-stratigraphic evolution of the rift and post-rift systems in the Northern Campos Basin, offshore Brazil. *Basin Research*, 2022, 1–33. <https://doi.org/10.1111/BRE.12674>
- Teboul, P.A., Durllet, C., Girard, J.P., Dubois, L., San Miguel, G., Virgone, A., Gaucher, E.C., & Camoin, G. (2019). Diversity and origin of quartz cements in continental carbonates: Example from the Lower Cretaceous rift deposits of the South Atlantic margin. *Applied Geochemistry*, **100**, 22–41. <https://doi.org/10.1016/J.APGEOCHEM.2018.10.019>
- Teixeira, J.B.G., Misi, A., & Silva, M.G. (2007). Supercontinent evolution and the Proterozoic metallogeny of South America. *Gondwana Research*, **11**, 346–361. <https://doi.org/10.1016/j.gr.2006.05.009>
- Temovski, M., Rinyu, L., Futó, I., Molnár, K., Túri, M., Demény, A., Otoničar, B., Dublyansky, Y., Audra, P., Polyak, V., Asmerom, Y., & Palcsu, L. (2022). Combined use of conventional and clumped carbonate stable isotopes to identify hydrothermal isotopic alteration in cave walls. *Scientific Reports*, 2022 121 12, 1–16. <https://doi.org/10.1038/s41598-022-12929-4>
- Trice, R. (2005). Challenges and insights in optimising oil production from Middle Eastern karst reservoirs. In: *SPE Middle East Oil and Gas Show and Conference*, Kingdom of Bahrain, March 2005, SPE-93679-MS. <https://doi.org/10.2118/93679-MS>
- Trindade, R.I.F., D'Agrella-Filho, M., Babinski, M., & Neves, B.B. (2004). Paleomagnetism and geochronology of the Bebedouro cap carbonate: evidence for continental scale Cambrian remagnetization in the São Francisco Craton, Brazil. *Precambrian Research*, **128**, 83–103.
- Tsykin, R.A. (1989). Paleokarst of the Union of Soviet Socialistic Republics. In: Bosák, P., Ford, D.C., Głazek, J., Horáček, I. (Eds.), *Paleokarst: A Systematic and Regional Review*. Vidala Academia, Praha, 253–295.
- van den Boorn, S.H.J.M., van Bergen, M.J., Vroon, P.Z., de Vries, S.T., & Nijman, W. (2010). Silicon isotope and trace element constraints on the origin of ~3.5 Ga cherts: Implications for Earth Archaean marine environments. *Geochimica et Cosmochimica Acta*, **74**, 1077–1103.
- Wei, D., Gao, Z., Fan, T., Niu, Y., & Guo, R. (2021). Volcanic events-related hydrothermal dolomitisation and silicification controlled by intra-cratonic strike-slip fault systems: Insights from the northern slope of the Tazhong Uplift, Tarim Basin, China. *Basin Research*, **33**, 2411–2434. <https://doi.org/10.1111/BRE.12562>
- Wray, R. A., & Sauro, F. (2017). An updated global review of solutinal weathering processes and forms in quartz sandstones and quartzites. *Earth-Science Reviews*, **171**, 520–557. <https://doi.org/10.1016/j.earscirev.2017.06.008>
- You, D., Han, J., Hu, W., Qian, Y., Chen, Q., Xi, B., & Ma, H. (2018). Characteristics and formation mechanisms of silicified carbonate reservoirs in well SN4 of the Tarim Basin. *Energy Exploration and Exploitation*, **36**, 820–849. <https://doi.org/10.1177/0144598718757515>
- Zhang, R. (1986). Sulfur Isotopes and Pyrite-Anhydrite Equilibria in a Volcanic Basin Hydrothermal System of the Middle to Lower Yangtze River Valley. *Economic Geology*, **81**, 32–45.
- Zhou, X., Chen, D., Qing, H., Qian, Y., & Wang, D. (2014). Submarine silica-rich hydrothermal activity during the earliest Cambrian in the Tarim basin, northwest China. *International Geology Reviews*, **56**, 1906–1918. <https://doi.org/10.1080/00206814.2014.968885>

Locality	Sample ID	Silica facies	Grain ID	$\delta^{30}\text{Si}$ (‰ NBS28)		$\delta^{18}\text{O}$ (‰ V-SMOW)	
Chapada Diamantina basement	CARB-1040	quartzite bedrock	16A	0.15	±0.17	13.58	±0.20
			16A-b1	0.12	±0.18	13.71	±0.19
			16B	0.3	±0.17	13.68	±0.18
			16B-b2	0.4	±0.19	13.73	±0.18
Calixto Cave	CARB-1081	qtz-I/chalcedony	19A	1.06	±0.17	24.95	±0.19
			19B	-0.52	±0.17	29.27	±0.20
	CARB-1063A	corroded chert	20A	0.95	±0.17	23.75	±0.20
			20B	-1.57	±0.20	24.18	±0.20
	CARB-1063B	qtz-I/chalcedony	21A	0.86	±0.18	26.05	±0.20
			21B	-0.12	±0.18	28.49	±0.19
	CARB-1098	chert	22A	0.98	±0.17	24.36	±0.27
			22A-b1	0.93	±0.14	23.47	±0.36
			22B	1.12	±0.20	23.56	±0.32
			22B-b2	1.07	±0.13	23.99	±0.38
	CARB-1085	chert	23A	1.48	±0.17	22.1	±0.36
			23B	0.88	±0.20	22.42	±0.36
	CARB-1094B	qtz-II corroded chert	25A	-1.9	±0.18	23.95	±0.19
			25B	0.84	±0.19	23.55	±0.19
	CARB-1094D	corroded chert	27A	0.49	±0.17	25.7	±0.36
			27B	0.65	±0.17	24.43	±0.37
	CARB-1094E	corroded chert	28A	-0.19	±0.20	24.14	±0.21
			28B	-1.09	±0.17	24.19	±0.19
	CARB-1094F	qtz-I/chalcedony	29B	-0.83	±0.17	29.72	±0.19
		qtz-II	29A	-1.4	±0.18	25.3	±0.20
	CARB-1094G	qtz-II	30A	-1.17	±0.17	26.84	±0.36
			30B	2.6	±0.17	28.41	±0.36
	CARB-1094H	highly corroded chert	31A	-2.98	±0.17	28.66	±0.36
			31A-b1	-2.63	±0.20	27.95	±0.38
			31B	-3.64	±0.17	28.29	±0.38
			31B-b2	-3.3	±0.18	25.98	±0.36

ID site	number of analyses per site	lated date	2 σ (Ma)	group
SiteD3-Mnz2	3	644	26	1
		604	34	
		619	31	
SiteA-Mnz1	2	1716	3	2
		-1402	-7	
SiteC-Mnz1	1	1186	46	
SiteMatrix4	2	1526	32	
		1508	82	
SiteA-Mnz2	2	2554	5	3
		2188	6	
SiteA-Mnz3	2	1973	5	
		1983	5	
SiteMatrix1	2	2006	20	
		1933	20	
SiteMatrix4	1	1942	30	
SiteMatrix3	6	2005	4	
		1994	4	
		1982	4	
		2010	4	
		2006	4	
		1962	5	

Silica facies	Texture	Primary inclusions T_h	Primary inclusions salinity (wt.%)	Description
qtz-mc	Microcrystalline quartz	<i>n.d.</i>	<i>n.d.</i>	Dolomite replacement; chert nodules and irregular bands; highly porous
qtz-C	Chalcedony or jigsaw mosaic quartz	<i>n.d.</i>	<i>n.d.</i>	Silica recrystallization texture; lining fractures and solutional vugs; gradual transition into qtz-I
qtz-br	Quartz-rich hydraulic breccias	160–185 °C	19–25	Quartz + K-feldspar + sericitic alteration involving overpressurization and hydraulic fracturing
qtz-I	Plumose-colloform megaquartz	<i>n.d.</i>	<i>n.d.</i>	Early stage of megaquartz precipitation, entrapping high temperature solid inclusions
qtz-II	Massive or zonal megaquartz	165–210 °C	17–25	Late stage of megaquartz precipitation